The Astrophysical Journal, 790:154 (16pp), 2014 August 1 doi:10.1088/0004-637X/790/2/154

THE COSMIC-RAY GROUND-LEVEL ENHANCEMENT OF 1989 SEPTEMBER 29

H. Moraal[1] and R. A. Caballero-Lopez[2]
[1] Centre for Space Research, School for Physical and Chemical Sciences, North-West University, Potchefstroom 2520, South Africa
[2] Ciencias Espaciales, Instituto de Geofisica, Universidad Nacional Autónoma de México, 04510 México D.F., Mexico
Received 2014 April 29; accepted 2014 June 18; published 2014 July 17

ABSTRACT

The ground-level enhancement (GLE) of 1989 September 29 is one of the largest of 71 solar energetic particle events observed by neutron monitors on Earth. It was smaller than the record-breaking GLE 5 of 1956 February 23, but by some measures it was larger than GLE 69 of 2005 January 20. It is also the most extensively studied of the 71 GLEs, and it was observed by more than 50 ground-based detectors in the worldwide network. This paper contains another study of the event, with the main difference from previous studies that all the existing observations are employed, instead of the usual selection of stations. An effort is made to represent all the information graphically. This reveals new insight in the event, mainly about its time profile. The main conclusion is that the event is the best example available of a "classical" GLE that has a gradual increase toward peak intensity and does not contain two or more distinct peaks as inferred previously. It does, however, suggest that there were two acceleration or release mechanisms: a prompt, rapid one and a delayed, slower one. This conclusion is based on a detailed comparison with GLE 69 of 2005 January 20, which is the best-known example of a double-peaked event with a "prompt" component. It is also found that the rigidity spectrum was probably softer than derived in several previous studies, and that the decay phase of the event reveals that the cosmic-ray diffusion coefficient in the neutron monitor range is proportional to rigidity.

Key words: acceleration of particles – Sun: coronal mass ejections (CMEs) – Sun: flares – Sun: heliosphere – Sun: particle emission

Online-only material: color figures

1. INTRODUCTION

Seventy-one ground-level enhancements (GLEs) of the cosmic-ray intensity have been recorded, with the first two detected in 1942 by ionization chambers operated in the USA, New Zealand, and Greenland by the Carnegie Institution of Washington. Neutron monitors that were established for the International Geophysical Year (1957) greatly increased the sensitivity of the worldwide network, and the general properties of the GLE were soon established. These properties were as follow: a rapid (<1 hr) rise to maximum intensity; a slower decay; strongly anisotropic fluxes early in the event, sometimes persisting throughout the event; and a rigidity spectrum that was much steeper than that of the galactic cosmic radiation, and which softened further throughout the event. It was also rapidly established that the majority of GLEs were observed following a major solar event on the western portion of the solar disk, later recognized to be a consequence of the spiral nature of the "Parker" heliospheric magnetic field (McCracken 1962c). These GLEs represent the highest-energy portion of the solar energetic particle (SEP) spectrum.

Originally, the generally accepted source mechanism for SEPs and GLEs was that they were produced in the lower solar corona, most probably by the solar flares observed immediately prior to the events. However, with the discovery of coronal mass ejections (CMEs; e.g.,Tousey 1973; MacQueen et al. 1974), and further systematic study of their nature since about 1990, the paradigm has shifted such that it is now generally accepted that the particles are accelerated by first-order *Fermi* acceleration (shock acceleration) in the shock front enveloping a CME (see, e.g., Gosling 1993). However, the time structure of some GLEs suggests that there may also be a more prompt acceleration mechanism, likely emanating from an impulsive flare-energy release in the upper chromosphere or lower corona.

The large GLE 69 of 2005 January 20 showed such an unusually fast increase to maximum intensity in ∼5 minutes, whereas the usual increase is more on the order of 30 minutes. Vashenyuk et al. (2006), McCracken et al. (2008), and several other authors identified two peaks for GLE 69, a prompt increase followed by a more usual gradual one. On the basis of timing in the event, the development of its spectrum with time, and the association with gamma rays emitted early in the event, McCracken et al. (2008) then concluded that the second, gradual increase was due to CME shock acceleration, but that the first, prompt increase was due to acceleration in the accompanying flare. This conclusion is not generally accepted, with authors such as Ruffolo et al. (2006) demonstrating that the complicated time structure of such events can be attributed to interplanetary propagation effects in a disturbed heliospheric magnetic field, or due to different apparent source locations, such as at the two foot points of large magnetic loops emanating from the Sun. This has, however, not yet been shown for GLE 69. Moraal & McCracken (2012) then highlighted the properties of five more GLEs in solar cycle 21 that showed this double-peak effect, while McCracken et al. (2012) studied the first, prompt peak in 10 of the largest events in the database of 71 events.

In view of this difference of opinion about the acceleration mechanism(s), we turned our attention to GLE 42 of 1989 September 29 because it is one of the largest events, and by far the best-observe done, being detected by 52 neutron monitors and 6 muon telescopes. Using data of several previous authors, Miroshnichenko et al. (2000) concluded that the event was the third largest GLE when measured in terms of >1 GV intensity; fifth largest if the fluence >30 MeV protons is used, but only the tenth largest in terms of >10 MeV fluence. They also noted that it was the first GLE observed by underground muon detectors, and that the intensity–time profile was notable for its nonclassic shape, showing a two-peak structure, which implies

the possibility of a two-component (or two-source) ejection of accelerated particles from the Sun. Finally, Miroshnichenko et al. stated that in spite of almost 10 yr of intensive studies, no generally accepted scenario existed at that time for the event, and many researchers were therefore still fascinated by its outstanding and challenging properties.

The event has been studied in at least 76 papers, cited in the exhaustive review of Miroshnichenko et al. (2000). In most of these papers, only a selection of neutron monitors is used (a notable exception being the paper of Lovell et al. 1998). However, that paper and most of the others do not display several features of the event graphically. This raises the question whether all the information in the event has been extracted. It is shown that due to our more detailed analysis we make a contribution to (a) the analysis of the increase-toward-peak phase of the event, (b) the spectral shape of the event and its evolution with time, (c) the use of lead-free neutron monitors (LFNM)—also called bare neutron monitors or neutron moderated detectors in the literature—to determine the spectral index, and (d) an assessment of the rigidity dependence of the cosmic-ray transport coefficients derived from the decay phase of the event.

According to Lovell et al. (1998) the source information about the event was that (a) solar flare activity was only indirectly detected from behind the western limb of the Sun, estimated at ∼25°S, 98°W; (b) types 2, 3, and 4 radio emission were observed in several time intervals ranging from 11:25 to 12:17, (c) soft X-ray emission with an intensity of X9.8 peaked at 11:33; and (d) a coronal mass ejection (CME) was observed by the coronagraph/polarimeter on the SMM satellite (Burkepile & St. Cyr 1993), in the vicinity of active region AR 5698, behind the western limb at approximately 25°S, 103°W. (All times in this paper are given as the time of observation at Earth, in UT.) Cliver et al. (1993) and Bhatnagar et al. (1996) estimated that the latitudinal span of the CME was as large as 77°, and that it had a high speed of 1828 km s^{-1}, with an extrapolated lift-off time at 11:21–11:22 UT. At 12:15 it had expanded to 4 solar radii. Cliver et al. (1993) also pointed out that if the longitudinal extent of the CME was comparable to the latitudinal extent, then, given the flare location of AR 5698, the CME could cover latitudes 60°W to 150°W. This includes the field line along the nominal Parker spiral field connecting Earth with a foot point at 60°W on the Sun. From the low Alfvén speed of 500 km s^{-1}, Cliver et al. inferred that the CME would drive a strong coronal/interplanetary shock.

It is a drawback for the analysis that no detailed heliospheric magnetic field or solar wind observations exist for the event. This limits the amount of information that can be extracted for the particle propagation phase toward Earth. However, the average geomagnetic K_p index from September 29 to October 4 was 2.2, indicating a relatively undisturbed geomagnetic field (well below the storm value of 5). These geomagnetic conditions were established by the heliospheric magnetic field that originated on the Sun between about September 26 and October 1. Smart et al. (1991) and Cliver et al. (1993) estimated that the solar wind speed during this period was a low 350 km s^{-1}. These observations indicate quiet heliospheric conditions, which is supported by neutron monitor observations. On the Sanae neutron monitor the variations in the six days prior to the event were smaller than 5%, while in the three days before the event they were limited to 1.8%. These variations are small compared to the modulation amplitude of ∼25% from solar minimum to solar maximum for this neutron monitor.

A second reason to revisit this event is that the magnitude and rigidity dependence of a GLE strongly depend on the yield of secondary particles that are produced in the atmosphere, and are recorded by instruments of different design. This yield function contains uncertainties, and these contribute to quantitative differences about the properties of the event, mostly about the form of the rigidity spectrum. Caballero-Lopez & Moraal (2012) therefore did a comprehensive re-evaluation of this yield function, both for galactic cosmic rays and for solar energetic particles (which produce the GLE). Using this yield function, we find that the spectrum of GLE 42 was softer than that derived in several of the previous studies. We also confirm the earlier experiences of, e.g., Bieber et al. (2002) and Oh et al. (2012) that the different yield function for neutron monitors without a lead producer, makes an important contribution to the calculation of the spectral shape of the event.

Sections 2–8 of the paper deal primarily with the temporal nature of the event, such as its onset time, rate of increase, and rate of decay. The findings of these sections are partially new, and the conclusions drawn from them about the nature of the event are sometimes different from those in previous studies. Sections 9 and 10, respectively, are about the anisotropy of the event and its rigidity spectrum as function of time. The basic results for these two aspects and the conclusions are similar to those of previous studies, but they contain quantitative refinements.

2. OVERALL CHARACTERISTICS OF THE GLE

The GLE of 1989 September 29 was observed by at least 50 neutron monitors, 2 neutron monitors without lead producer (LFNM), and 6 muon telescopes (MT). There may be more observations, but these are the stations available in the database described by McCracken et al. (2012).

Data from the following stations were used in the study: Apatity (cutoff rigidity $P_c < 1$ GV), Barentzburg (<1 GV), Cape Schmidt (<1 GV), Fort Smith (<1 GV), Goose Bay (<1 GV), Goose Bay MT (<1 GV), Inuvik (<1 GV), Inuvik MT (<1 GV), Mawson (<1 GV), McMurdo (<1 GV), Mirny (<1 GV), Nain (<1 GV), Norilsk (<1 GV), Oulu (<1 GV), South Pole (<1 GV), South Pole LFNM (<1 GV), Terre Adelie (<1 GV), Thule (<1 GV), Tixie Bay (<1 GV), Deep River (1.02 GV), Deep River MT (1.02 GV), Sanae (1.06 GV), Sanae LFNM (1.06 GV), Calgary (1.08 GV), Ottawa (1.08 GV), Kergeulen (1.19 GV), Mt. Washington (1.24 GV), Durham (1.41 GV), Yakutsk (1.7 GV), Kingston (1.84 GV), Hobart (1.88 GV), Mt. Wellington (1.89 GV), Newark (1.97 GV), Magadan (2.09 GV), Kiel (2.29 GV), Moscow (2.46 GV), Moscow MT (2.46 GV), Novosibirsk (2.91 GV), Climax (3.03 GV), Dourbes (3.24 GV), Larc (3.40 GV), Kiev (3.62 GV), Irkutsk (3.66 GV), Lomnicky Stit (4.0 GV), Jungfraujoch IGY (4.48 GV), Jungfraujoch NM64 (4.48 GV), Bern (4.49 GV), Hermanus (4.9 GV), Baksan (5.6 GV), Gran Sasso, Gran Sasso M1, Gran Sasso M2, Gran Sasso M3, Gran Sasso M4 (6.10 GV), Campo Imperatore (6.32 GV), Rome (6.32 GV), Alma Ata A (6.66 GV), Alma Ata B (6.69 GV), Tbilisi (6.91 GV), Potchefstroom (7.35 GV), Erevan (7.6 GV), Samarkand (7.65 GV), Mexico City (8.15 GV), Athens (8.72 GV), Tsumeb (9.29 GV), Mt. Norikura (11.39 GV), Mt. Norikura MT (11.39 GV), Tokyo-Itabashi (11.61 GV), Nagoya MT (12.1 GV), and Darwin (14.19 GV). Most of these stations were tabulated by Lovell et al. (1998). The design and location details of these neutron monitors are listed in Shea & Smart (2000). This is the

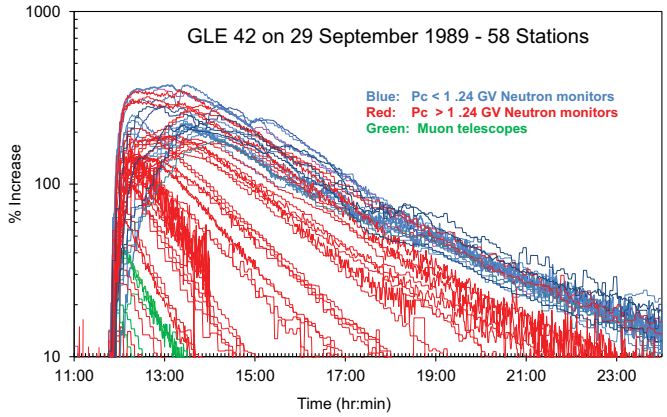

Figure 1. GLE as observed by 50 neutron monitors, 2 LFNMs, and 6 muon telescopes. Stations with geomagnetic cutoff rigidities $P_c < 1.24$ GV are shown in blue. All these stations have an effective atmospheric cutoff of 1 GV (when at sea level). Stations with $P_c > 1.24$ GV are shown in red. The lowest red curve just visible after 12:00 is for Darwin, with $P_c = 14.2$ GV. Muon telescopes are shown in green (details given in Figure 4). The time resolution on most stations is 5 minutes, with 1 minute resolution on some stations.

(A color version of this figure is available in the online journal.)

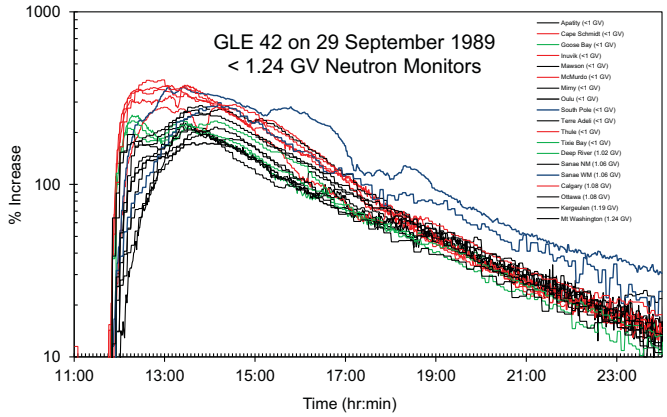

Figure 2. Event as observed by 20 neutron monitors with cutoff rigidity $P_c < 1.24$ GV. All these stations have an effective atmospheric cutoff rigidity ≈1 GV (except South Pole, for which it is significantly smaller due to its altitude at ≈3000 m). Differences are primarily due to different asymptotic directions of viewing.

(A color version of this figure is available in the online journal.)

most comprehensive neutron monitor list available, consisting of 219 entries. (Due to updates in design and changes in location, there may be more than one entry per station.)

Figure 1 shows the event as observed by these detectors. The figure gives the percentage increase above the ambient cosmic-ray counting rate at each station. Stations with geomagnetic cutoff rigidities $P_c < 1.24$ GV are shown in blue. These stations are subject to the atmospheric cutoff rigidity $P_a \approx 1$ GV at sea level. This implies that these stations see essentially the same spectrum, and there are no effects due to different energy or rigidity responses. All differences are due to differences in the viewing direction of the detectors. (The South Pole neutron monitor and LFNM at altitude ≈3000 m have a significantly lower atmospheric cutoff. Where important for the analysis, this will be pointed out.) Stations with $P_c > 1.24$ GV are shown in red. The muon telescopes are in green. The time resolution on most stations is 5 minutes, with 1 minute resolution on some.

For clarity and for later use, Figures 2 and 3 show the $P_c < 1.24$ GV stations and $P_c > 1.24$ GV neutron monitors separately. The muon telescopes are shown separately in Figure 4.

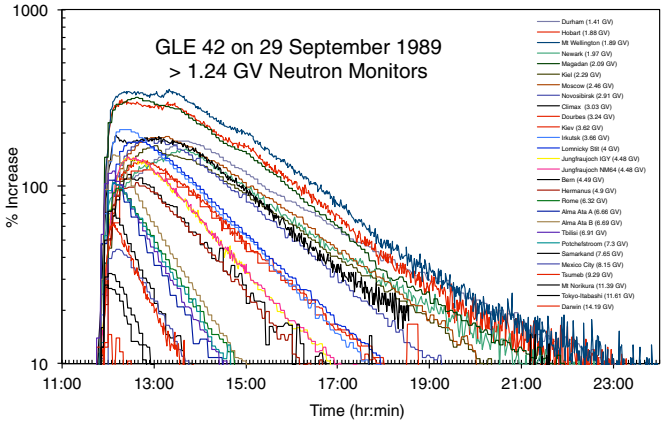

Figure 3. Increase as observed by 28 neutron monitors with geomagnetic cutoff rigidity P_c larger than the atmospheric cutoff of ≈1 GV. The Gran Sasso neutron monitors which have data only up to 14:00, as well as the muon telescopes, are excluded. The increases become smaller with increasing P_c, with the smallest increase at Darwin, $P_c = 14.2$ GV, just visible between 12:00 and 12:30. The top three curves are for Mt. Wellington, $P_c = 1.89$ GV (blue); Hobart, $P_c = 1.88$ GV (red); and Magadan, $P_c = 2.09$ GV (green). The next group of five curves are from the top: Durham, $P_c = 1.41$ GV (blue); Newark, $P_c = 1.97$ GV (green); Kiel, $P_c = 2.29$ GV (black); and Novosibirsk, $P_c = 2.91$ GV (blue).

(A color version of this figure is available in the online journal.)

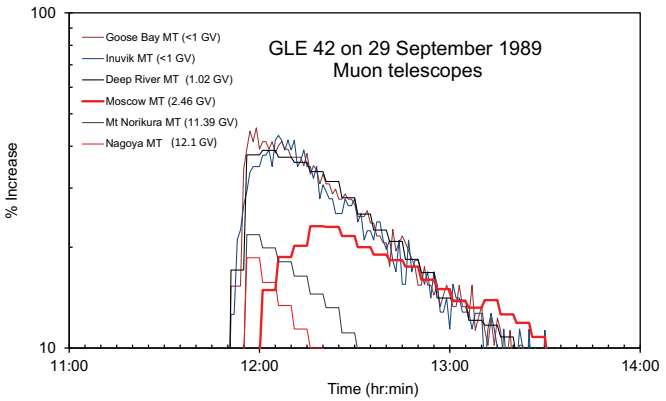

Figure 4. Increase as observed by six muon telescopes. The top three are for the muon telescopes at Deep River, Inuvik, and Goose Bay, all three at $P_c \approx 1$ GV. The two bottom curves are for Mt. Norikura at $P_c = 11.4$ GV and Nagoya at $P_c = 12.1$ GV. The heavy trace is for the Moscow muon telescope at $P_c = 2.46$ GV.

(A color version of this figure is available in the online journal.)

The general trend, which can be seen best from Figure 2, is a fast rise from the onset at ≈11:45, reaching peak intensity at ≈12:15 at some stations, and as late as ≈13:45 at others. Thereafter there is a quasi-exponential decay with a decay rate that increases with increasing cutoff rigidity. The event remained visible to at least 06:00 on the next day (data not shown beyond 24:00).

The peak intensities in Figure 3 are generally ordered according to cutoff rigidity of the stations. The top three curves are for Mt. Wellington, $P_c = 1.89$ GV (blue); Hobart, $P_c = 1.88$ GV (red), and Magadan, $P_c = 2.09$ GV (green). The Mt. Wellington peak intensity is larger than the Hobart one (even though its cutoff rigidity is slightly higher), because Mt. Wellington monitor is located at higher altitude and the increases shown in this figure have not been corrected to sea level. The correction factors to sea level for these three NMs are 0.88, 0.96, and 0.78, respectively. The next group of 5 curves are from the top: Durham, $P_c = 1.41$ GV (blue), Moscow, $P_c = 2.46$ GV (brown),

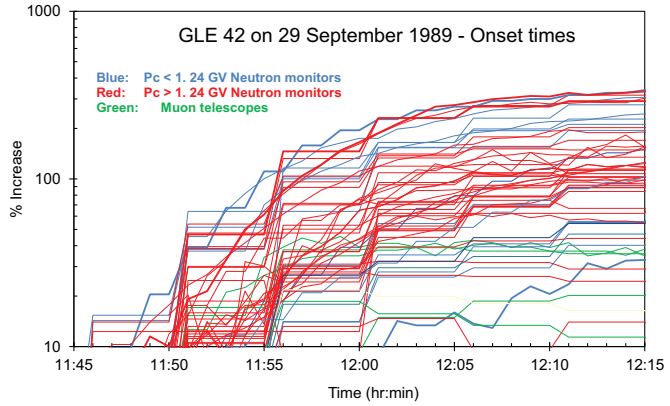

Figure 5. Onset phase of the event. The 10% level is reached in the interval 11:45–11:50, with Thule (heavy blue line; time resolution 1 minute), indicating that it was at 11:48. The second- and third-fastest onsets were at Magadan (heavy red; 5 minute resolution) and Mt. Wellington (heavy red; 1 minute resolution). The two latest starters were Mawson (bottom heavy blue line) and Moscow muon telescope (green) which went past the 10% level at 12:02 and 12:01, respectively.

(A color version of this figure is available in the online journal.)

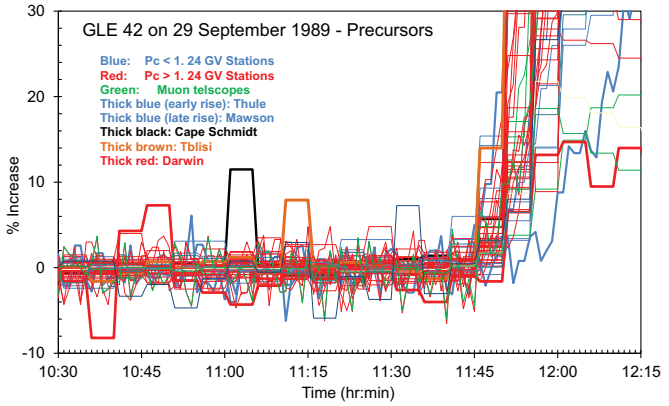

Figure 6. Precursors of the event. The thick black feature between 11:00 and 11:05 is for Cape Schmidt. The thick brown one between 11:10 and 11:15 is for Tblisi, and the thick red one between 10:35 and 10:50 for Darwin.

(A color version of this figure is available in the online journal.)

Newark, $P_c = 1.97$ GV (green), Kiel $P_c = 2.29$ GV (black), and Novosibirsk, $P_c = 2.91$ GV (blue). The lowest curve just visible after 12:00 is for Darwin, with $P_c = 14.2$ GV. Throughout the paper the increases at South Pole, Mt. Washington, Calgary and Sanae have been multiplied by factors of 0.6, 0.7, 0.84, and 0.84 to allow for altitude effects, as described by Caballero Lopez & Moraal (2012) and earlier reference therein. (Other stations at altitude that are not used for quantitative purposes are not similarly corrected.)

The detailed information in Figure 2 is as follows. (1) Five stations show a prompt increase, reaching the peak intensity in ≈27 minutes, from 11:48 to 12:15. At 12:15 they are from the top: Thule (red), Cape Schmidt (blue), Inuvik (green), Calgary (blue), and Goose Bay (green). There are several stations that show a much slower increase, reaching the peak value only about 2 hr after onset, at ≈13:45. From the bottom upward at 13:00 they are Sanae (blue), Mawson (red), SanaeLFNM (blue), and Oulu (magenta). Before 12:25 Mawson (red) and Mirny (black) have the lowest intensity, and we consider them as the lowest risers. The details of the increase phase will be shown in higher resolution in Figures 5 and 6. The highest blue curve in Figure 2 for times >18:00 is for the Sanae LFNM, at $P_c = 1.02$. Its gradual rise above the other $P_c < 1.24$ GV neutron monitors is due to the fact that it is more sensitive to lower energy particles. (The South Pole LFNM is not visible in-between the other neutron monitors.) Although these instruments are positioned at the same cutoff rigidity as their companion neutron monitors, they respond more to lower energies than the neutron monitors. Therefore, their increases are typically larger, and the rate of decay is lower. In Section 9, it will be shown that these two detectors make an important contribution to the determination of the spectral shape of the event.

McCracken et al. (2012) defined the decay time as the time needed to decrease to 50% of the peak intensity. They found that the average decay time for the 10 largest GLEs observed was $T_d = 101$ minutes. For comparison, Figure 2 shows that at $P_c \approx 1$ GV, the decay time for this event is $T_d \approx 120$ minutes, which is representative of the average value. This rate of decay was different and time variable for the different stations until ≈18:40. After that time the intensities had reached the same level within ±15% on all neutron monitors. We interpret the early variability as due to injection and beaming effects which cause time variation and anisotropy. These effects stopped at ≈18:00. In Section 7, it will be shown how the decay rate as function of cutoff rigidity can be used to determine the rigidity dependence of the cosmic-ray diffusion coefficient in the inner heliosphere.

3. MUON TELESCOPES

Figure 4 shows the event as seen by six muon telescopes, at Goose Bay ($P_c < 1$ GV), Inuvik (<1 GV), Deep River (1.02 GV), Moscow (2.46 GV), Mt. Norikura (11.39 GV), and Nagoya (12.1 GV). The heavy trace for the Moscow muon telescope is highlighted because it is clearly different, being significantly delayed relative to the others.

Muon telescopes respond to much higher energies than neutron monitors. The upper green traces in Figure 1 show, for instance, that the increases for $P_c < 1$ GV muon telescopes lie between the neutron monitor increases at Tsumeb at $P_c = 9.29$ GV and Mount Norikura at $P_c = 11.4$ GV. Furthermore, the increases on the $P_c \approx 1$ GV muon telescopes is only about three times larger than those on Mt. Norikura and Nagoya, while the same ratio for neutron monitors is ≈20 times. This indicates that muon telescopes respond to much higher rigidities than neutron monitors. The rigidity response of a detector is captured in its atmospheric-plus-instrumental yield function, recently reviewed by Caballero-Lopez & Moraal (2012). These yield functions are such that a neutron monitor at $P_c = 1$ GV has median rigidity of response $P_{\rm med} = 16.7$ GV (above and below which half the counting rate is contributed) if the particles are galactic cosmic rays with a relatively hard spectrum. For solar energetic particles, with much softer spectra, this value is much lower. If the particle intensity spectrum is of the power-law form $P^{-\gamma}$, then it follows from the results of Caballero-Lopez & Moraal (2012) that the median rigidity for a neutron monitors is given by

$$\begin{aligned} P_{\rm med}(\gamma = 4) &= 1.47[2.38^{2.15} + P_c^{2.15}]^{(1/2.15)}, \\ P_{\rm med}(\gamma = 5) &= 1.30[1.62^{2.27} + P_c^{2.27}]^{(1/2.27)}, \\ P_{\rm med}(\gamma = 6) &= 1.21[1.31^{2.34} + P_c^{2.34}]^{(1/2.34)}. \end{aligned} \quad (1)$$

For a neutron monitor at $P_c = 1$ GV, this gives $P_{\rm med}(\gamma = 4) = 3.7$ GV, $P_{\rm med}(\gamma = 5) = 2.4$ GV, and $P_{\rm med}(\gamma = 6) = 1.9$ GV. However, the median rigidities of response for the

Mount Norikura neutron monitor at $P_c = 11.4$ GV are $P_{\rm med}(\gamma = 4) \approx 17.0$ GV, $P_{\rm med}(\gamma = 5) \approx 14.9$ GV, and $P_{\rm med}(\gamma = 6) \approx 13.8$ GV. This is then also approximately the median rigidity for the $P_c < 1$ GV muon telescopes. Given this correspondence, the muon telescopes add no further insight into the time profile and the rigidity dependence of the event.

The exception to this statement is the delayed increase and slower decay on the Moscow muon telescope, which we will interpret in terms of asymptotic directions of viewing in Section 8.

Miroshnichenko et al. (2000) mention that for this event bursts of muons were seen by underground muon telescopes which have even larger median rigidities. These are, however, not included in our database.

This muon telescope response is unique because in our search through the database we could not find other GLEs for which muon telescopes have measured statistically significant increases over a significant timescale with a well-resolved time profile.

4. ONSET PHASE

The onset phase of a GLE contains information about the nature of the source(s) and acceleration mechanism(s) that produce the event. Several authors have identified prompt and delayed peaks in GLEs, and these have mostly been attributed to two effects. First, double or multiple peaks may be attributed to interplanetary propagation effects (e.g., Ruffolo et al. 2006 and references therein), where particles can reach Earth on different propagation paths. Second, there may more than one acceleration mechanism, such as a flare and a CME shock, as was proposed for GLE 69 of 2005 January 20 by Vashenyuk et al. (2006, 2011) and McCracken et al. (2008).

Figure 5 shows the onset phase of the event in detail. The 10% increase level occurred in the interval 11:45–11:50, with Thule (heavy blue line; time resolution 1 minute), indicating that it was at 11:48. The second- and third-fastest onsets were Magadan (heavy red; 5 minute resolution) and Mt. Wellington (heavy red; 1 minute resolution). The two latest starters were Mawson (bottom heavy blue line) and Moscow muon telescope (green) which went past the 10% level only at 12:02 and 12:01, respectively. The behavior of these two stations can be understood as a "fill-in" effect due to increasing amounts of scattering with time, e.g., Cramp et al. (1993) and Lovell et al. (1998): stations that look opposite from the directed beam will only respond to scattered particles from the "backward" direction. Except for these two stations, the others went above 10% in the 7 minute interval 11:48–11:55. Bearing in mind that the time resolution on most stations is 5 minutes, we infer that the onset data indicate a single initial acceleration mechanism.

The onset of the event indicates that the original acceleration phase is probably not due to the shock that envelopes the expanding CME. There are two reasons for this. First, as will be discussed in Section 7 and Figure 9, the onset phase of the event is highly anisotropic. First-order *Fermi* or shock acceleration depends on the scattering of particles across the shock multiple times before they escape, receiving an acceleration boost with every crossing. This requires high levels of turbulence on both sides of the shock. Such turbulence will destroy the anisotropy of the event, which is contrary to observation.

The second reason that makes shock acceleration in the initial stage unlikely is that if there was sufficient turbulence for it to be effective, the rapid rate of increase implies diffusion coefficients that are a few orders of magnitude smaller than inferred otherwise. In collisionless shock acceleration, the acceleration time should be proportional to rigidity P (e.g., Drury 1983). The propagation time to Earth should be proportional to particle speed (expressed as $\beta = v/c$, i.e., as fraction of the speed of light). Consequently, the time dispersion in the onset time of the event should be proportional to P/β. The minimum rigidity is the cutoff rigidity of polar stations, $P_{\rm c} \approx 1$ GV. The more appropriate number is median rigidity $P_{\rm med} \approx 3$ GV, for which $\beta = 0.95$. Hence, there should be insignificant (<1 minute) propagation delay in the onsets, but the acceleration time, τ_a, for the high cutoff stations should be ≈6 times longer than for the polar stations. From Figure 5, the maximum difference in onset time is ≈7 minutes. These two numbers then imply that the acceleration time at the lowest rigidity ($P_{\rm med} \approx 3$ GV) is <1.4 minutes. Expressed as function of rigidity it is $\tau_a < 0.47P$ minutes. This is an upper limit because the onset times are not ordered according to cutoff rigidity, but are rather randomly scattered in the time interval 11:48–11:55.

In first-order *Fermi* (or shock) acceleration in a quasi-parallel configuration, the acceleration timescale τ_a is of the order of κ/V_s^2, where κ is the diffusion coefficient due to pitch-angle scattering of the particles along the magnetic field lines, and V_s the shock speed. The observed upper limit for τ_a, together with an assumed value of V_s, therefore enables one to estimate the value of κ in the acceleration process. Using the observed shock speed $V_s = 1828$ km s^{-1}, this leads to $\kappa \sim \tau_a V_s^2 < 1.6 \times 10^{16} \beta P$ cm^2 s^{-1}. Caballero-Lopez et al. (2004) determined that the typical diffusion coefficient at radial distance >1 AU, that describes the long-term modulation of galactic cosmic rays, is $\kappa \sim 4 \times 10^{22} \beta P$ cm^2 s^{-1}. Diffusion coefficients should scale approximately inversely proportional to B, and in the inner heliosphere the Parker spiral magnetic field scales as r^{-2}. Thus, the diffusion coefficient at 2 solar radii or 0.01 AU, which is the typical distance where CME shocks have developed, should be $\sim 10^4$ smaller than at Earth, i.e., $\kappa \sim 4 \times 10^{18} \beta P$ cm^2 s^{-1}. This is 250 times the upper limit derived from the maximum onset dispersion above. Hence, we regard CME shock acceleration for the initial onset phase (about the first 5 minutes) as unlikely. This conclusion must bear in mind, however, that across the curved shock front of a CME the magnetic field geometry will range from parallel to perpendicular relative to the shock front. The diffusion coefficient perpendicular to the field is typically one to two orders of magnitude smaller than the parallel coefficient (e.g., Giacalone & Jokipii 1999). In addition, the acceleration timescale may be reduced further by self-excitation of waves (e.g., Ng & Reames 2008).

5. PRECURSORS

Precursors are sometimes observed prior to the main phase of an event. They typically happen due to relativistic neutrons that are accelerated right at the initial phase of the event and then propagate on a straight-line trajectory to Earth, as first observed by Chupp et al. (1987). Four such definite solar neutron events have been observed (listed in Moraal et al. 2000; see also Bieber et al. 2005). We examined the event for such precursors in Figure 6. The neutron monitor increases generally fluctuate with ±2% about zero. The only possibly significant example of precursors we could find was on Cape Schmidt which recorded a 10.3% increase in the interval from 11:00 to 11:05, Tblisi 7.9% between 11:10 and 11:15, and Darwin 7.3% between 10:45 and 10:50. There were no other similar increases in the period back to 08:00. Since the three events do not coincide in time, and since they are accompanied by decreases of the same order of

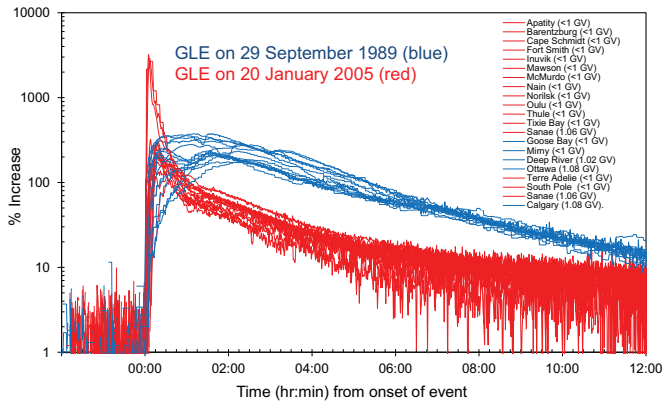

Figure 7. Comparison of GLEs 42 and 69. Only stations with cutoff rigidity smaller than the atmospheric cutoff are used. The horizontal axis is plotted as time from the onset of the event.

(A color version of this figure is available in the online journal.)

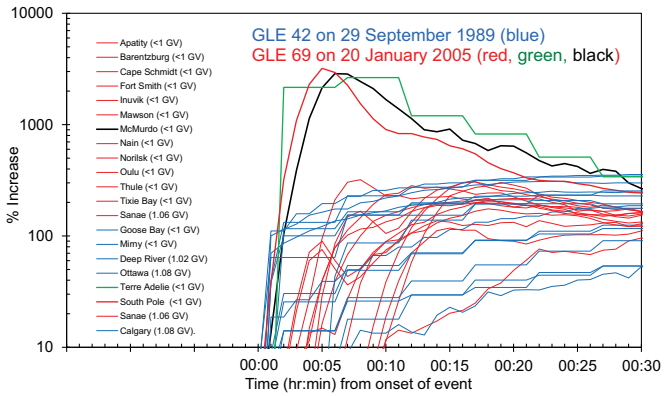

Figure 8. Same as Figure 7, but focusing on the onset and peaks of the events. The top red, green, and black curves are for GLE 69 as observed by South Pole, Terre Adelie, and McMurdo, respectively.

(A color version of this figure is available in the online journal.)

magnitude, we conclude that the event did not have significant precursors.

This finding is in contrast to previous studies where Takahashi et al. (1990) reported an increase at 11:42 on Mt. Norikura and Tokyo; Alessio et al. (1991) a 7.0% increase at 11:45–11:47 on Campo Imperatore; and de Koning (1994) 9.1% at 11:00–11:05 on Alma Ata; 9.1% at 11:00–11:15 on Tblisi; 24% at 11:50–11:55 on Novisibirsk; and 3.4% at 11:40–11:45 on Oulu.

6. COMPARISON WITH GLE 69 OF 2005 JANUARY 20

The nature of the event can be better understood by comparing it to others. This is done in Figures 7 and 8 which compare the event with that of 2005 January 20. The two figures show that the two events are qualitatively different. Overall, GLE 42 has a relatively long rise time of ≈30 minutes while GLE 69 raises to its peak intensity in ≈5 minutes, after which it has a much more rapid decay then GLE 42.

After the initial onset phase of less than 5 minutes, discussed in Section 4, the subsequent rise to peak intensity is fairly gradual, between 30 and 90 minutes. This suggests that the main phase of the event was caused by a single acceleration, probably by the shock that envelops a coronal mass ejection (CME), which is the current paradigm for the acceleration of solar energetic particles (SEPs). GLEs such as 69 also show an earlier, much more prompt, increase with a rise time that may be up to 10 times shorter than that for the gradual event. Moraal & McCracken (2012) identified six such GLEs in solar cycle 23, including GLE 42. Some authors, e.g., Shea & Smart (1996, 1997), Vashenyuk et al. (1994), and McCracken et al. (2008, 2012), proposed that this fast-rising component is accelerated in other sources lower in the solar corona. The rise-time to peak intensity for this prompt phase is typically only a few minutes, while for the delayed phase it maybe an order of magnitude longer, even more than one hour. In a case such as GLE 69 of 2005 January 20, some neutron monitors even showed a clear decrease between the first and second increases, suggesting two separate injection and/or acceleration mechanisms. McCracken et al. (2008) used several arguments to propose that for GLE 69 the prompt phase was caused by acceleration in the accompanying flare near the solar surface, while the delayed phase was due to acceleration in the subsequent CME (with an estimated speed of 3700 km s^{-1}).

The second major difference between the GLEs 42 and 69 is the decay phase. This will be studied quantitatively in Section 7: the overall characteristics are that GLE 42 showed a quasi-exponential decay with a characteristic or *e*-folding time of 5 hr. (In the earlier phases, before ≈18:00, this decay was detector-dependent.) On the other hand, GLE 69 clearly had two decay phases, with a very rapid decay, with characteristic time of ≈10 minutes in the first hour of the event. From then on, the decay was similar to that of GLE 42, until there was a flattening-off in the late phases beyond about 6 hr.

The similarity in decay of the two events more than an hour after onset indicates that interplanetary propagation conditions were similar for the two events. Hence, the rapid fall-off of GLE 69 in the first hour cannot be attributed to different propagation conditions than for GLE 42. McCracken et al. (2008) interpreted this rapid initial decay as the switch-off of the first of two acceleration mechanisms, likely to be the solar flare that was observed during the event.

It is equally important that the expanded initial phases in Figure 8 show that the initial rises were very similar—both events reached the 100% level in the first ≈2 minutes. Thereafter, only three stations (South Pole, Terre Adelie, and McMurdo) in GLE 69 continued to rise rapidly, but the others did not. This indicates that there was an extremely anisotropic beam of particles in this phase of GLE 69. However, GLE 42 continued to rise much slower, with much less anisotropy, for the next hour, before it started to decay.

The following synthesis can be constructed from the combination of the rates of increase, the different peak structures and the two-step decay of GLE 69: in the initial few (<5) minutes there was a very rapid acceleration phase that was similar in both events. After this time this initial mechanism in GLE 42 was overwhelmed by a more gradual acceleration for at least the next hour. This second acceleration mechanism was probably also present in GLE 69, but its effect remained submerged below that of the first acceleration. After ≈5 minutes, the first, prompt acceleration cut off in GLE 69, and the beam decayed rapidly for an hour, until it met the intensity level that is inferred to have been produced by the second, more gradual acceleration. It is generally agreed that the second, more gradual acceleration, is due to shock acceleration in the CME, and this supports the conclusion of McCracken et al. (2008) that the first acceleration originated in the solar flare. The qualitative difference between the two events is that for GLE 69 the first acceleration was dominated by the second one, while for GLE 42 it was the

other way round. This is in accord with the fact that GLE 69 was associated with a well-identified solar flare that was well-connected to Earth via the nominal Parker spiral magnetic field, while for GLE 42 a flare could only be indirectly inferred behind the western limb of the Sun. However, as mentioned before, the accompanying CME for GLE 42 had such a large angular extent that it was probably well-connected to Earth. Hence, these angular differences provide an explanation for the difference in the relative strengths of the two mechanisms in the two events. Finally, it seems natural that the particles produced in the first acceleration were seed particles for the second acceleration.

The difference in the relative contributions of these two accelerations in the two events, produced a fairly "classical" time profile for GLE 42 with a significant anisotropy, while GLE 69 was a very rapid, extremely anisotropic event, with two peaks.

This conclusion is in contrast to that of de Koning (1994), de Koning & Bland (1995), de Koning & Mathews (1996), and Miroshnichenko et al. (2000), who inferred a double-source mechanism for GLE 42. These authors could not do the comparison with GLE 69 on 2005 January 20, but they based their conclusion primarily on the two observations that (a) there were two clear peaks in some stations, (the green traces in Figure 2), and (b) stations with $P_c > 2$ GV only saw the first peak. This is different from our inferences above, and in Section 8, where we discuss the anisotropy of the event, we argue that there are alternative explanations for these two effects.

7. DECAY RATE AND RIGIDITY DEPENDENCE OF COSMIC-RAY TRANSPORT COEFFICIENTS

The well-observed decay of GLE 42 offers an excellent opportunity to study the transport of energetic particles in the heliosphere, well after complications that may be introduced during the acceleration phase. In particular, because the spectrum was so hard, these decays were better observed at high cutoff stations than for any other GLE. The decay can be used explicitly to determine the spatial and rigidity dependence of the cosmic-ray diffusion coefficient.

In the late phase of the event, where the particle beam has been significantly scattered, and where adiabatic focusing of the anisotropic beam is not important any more, the diffusive model for cosmic-ray transport can be used. The well-known Parker (1965) cosmic-ray transport equation for the omnidirectional distribution function, f, in this limit is

$$\frac{\partial f}{\partial t} + V\cdot\nabla f - \nabla\cdot(K\cdot\nabla f) - \frac{1}{3}(\nabla\cdot V)\frac{\partial f}{\partial \ln p} = 0. \quad (2)$$

Here $\boldsymbol{V}$ is the solar wind velocity and $\boldsymbol{K}$ is the diffusion tensor in the heliospheric magnetic field, containing symmetric elements that describe diffusion along and perpendicular to the magnetic field, and off-symmetric elements for gradient and curvature drift in this field. The equation is expressed as function of particle momentum, p, which is related to rigidity by $P = pc/Ze$, where Z is charge number. The details are summarized by Moraal (2013). In the lowest-order approximation of spherical symmetry, this equation reduces to

$$\frac{\partial f}{\partial t} = \frac{1}{r^2}\frac{\partial}{\partial r}\left[r^2\left(\kappa\frac{\partial f}{\partial r} - Vf\right)\right] + \frac{2V}{3r}\frac{\partial f}{\partial \ln p}. \quad (3)$$

The second term within the square brackets is the convective term. It is smaller than the first, diffusive term if the radial gradient $g \equiv f^{-1}\partial f/\partial r > V/\kappa$. According to the well-known Palmer consensus (Palmer 1982), typical values for the diffusion mean free path, $\lambda = 3\kappa/v$, lie in the range $0.08 < \lambda(\mathrm{AU}) < 0.3$. These values are valid up to rigidities of about 1 GV. The smallest value of λ implies that g must be larger than 0.4%, which is certainly always met for a GLE. Next, if f is a power law of the form $f \propto p^{-\gamma}$ and $\gamma \sim 2$, the third, adiabatic, term is of the same order as the convective term. Hence, the transport equation reduces to the standard diffusion equation

$$\frac{\partial f}{\partial t} = \frac{1}{r^2}\frac{\partial}{\partial r}\left[r^2\kappa\frac{\partial f}{\partial r}\right]. \quad (4)$$

If the diffusion coefficient is of the form $\kappa = \kappa_0(r/r_0)^\alpha$ (and hence the diffusion mean free path $\lambda = 3\kappa/v$ is of the same form: $\lambda = \lambda_0(r/r_0)^\alpha$), the solution for an impulsive injection at $r = 0$ and $t = 0$ is (e.g., Duggal 1979)

$$f \propto t^{3/(\alpha-2)}\exp\left[\frac{r^{2-\alpha}}{(2-\alpha)^2\kappa_0 t}\right]. \quad (5)$$

This diffusive profile has the property that the tail of the increase, determined by the first, power-law part, is sensitive to the exponent α, but not the magnitude κ_0. The beginning phase, determined by the second, exponential part does, however, explicitly depend on κ_0. Since the values derived for GLEs are for radial distances typically <1 AU, the values are best representative of the diffusion coefficient or mean free path parallel to the background magnetic field, i.e., $\boldsymbol{\kappa}_\parallel$ or $\boldsymbol{\lambda}_\parallel$.

Figures 9(a) and (b) show this solution for GLE 42 in blue, and for GLE 69 in red. For GLE 42 only the fastest (Thule) and slowest (Mawson) observed increases are plotted. The top and bottom blue curves are, respectively, the best fits to these two increases, with diffusion mean free paths $\lambda = 0.22r^{0.9}$ AU and $\lambda = 0.17r^{0.9}$ AU. The two diffusion mean free paths needed indicate the degree of deviation from a spherically symmetric impulsive release at $r = 0$. This difference is mainly due to anisotropy of the event as described in the next section, but the two curves demonstrate that the event can be fairly well described by a spherically symmetric diffusion model, which is typical of a CME extended over a large solid angle, as was observed (e.g., Cliver et al. 1993).

For GLE 69 the situation is much different. The fastest (Terre Adelie) and slowest (Thule) risers are again plotted, this time in red. Here the top and bottom fits are, respectively, for $\lambda = 0.23r^{-0.4}$ and $\lambda = 0.047r^{-0.4}$ AU. However, close inspection in Figure 9(b) shows that during the first half hour of the event, these two diffusive model curves cannot fit the observed profiles nearly as well as for GLE 42. Because the flare associated with GLE 69 was well-connected along the nominal Parker spiral magnetic field to Earth, the very sharp initial peak should rather be interpreted as due to a non-CME origin. McCracken et al. (2008) identified this as flare acceleration.

The same analysis can be applied to the time profiles of neutron monitors at $P_c > 1$ GV, shown in Figure 3. It shows, however, that for these rigidities the decays are quasi-exponential in nature, of the form $f = f_p\exp(-t/t_d)$, with t_d the characteristic decay time. Hence, we follow the simpler procedure to calculate these decay times from the slopes of the profiles in Figure 3. Their values are shown as function of cutoff rigidity and median rigidity (for $\gamma = 5$ in Equation (1)) in Figure 10. In this case, Equation (4) becomes $\partial f/\partial t = f/t_d$, and hence the rigidity dependence of t_d reflects the

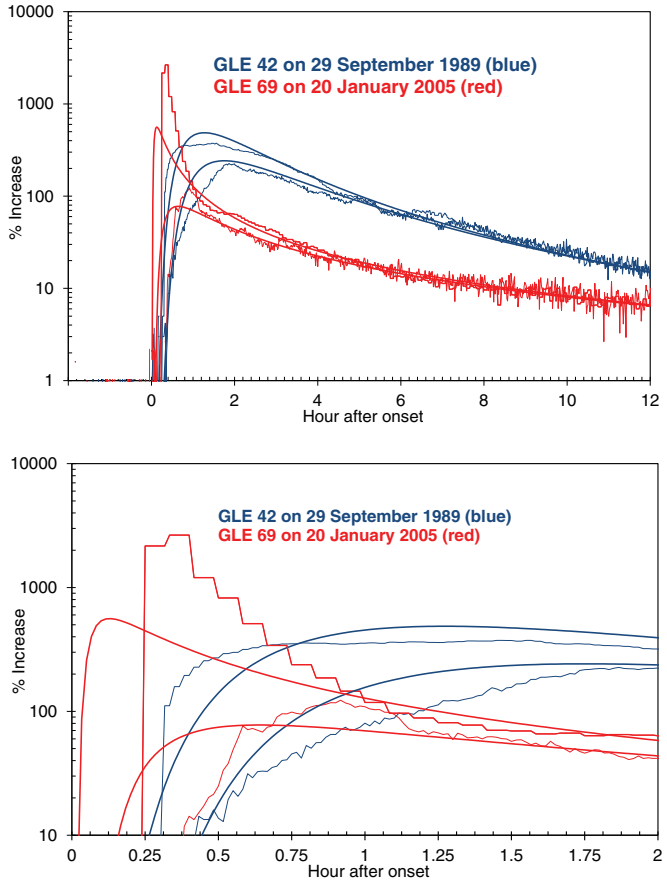

Figure 9. Diffusive fits to GLE 42 and GLE 69. For GLE 42 the fastest and slowest risers shown are Thule and Mawson. Panel b is a higher-resolution expansion of panel (a) for the initial phase. The top and bottom blue curves are for $\lambda = 0.22r^{0.9}$ AU and $\lambda = 0.17r^{0.9}$ AU. For GLE 69 the fastest and slowest risers shown are Terre Adelie and Thule. The top and bottom red curves are for $\lambda = 0.23r^{-0.4}$ AU and $\lambda = 0.047r^{-0.4}$ AU.

(A color version of this figure is available in the online journal.)

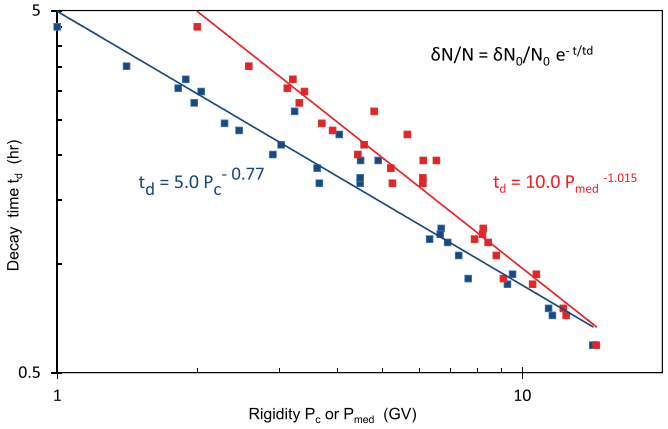

Figure 10. Decay time of the increases plotted as function of cutoff (blue) and median (red) rigidity. The values are read off from the slopes in Figures 1 and 2. For the 1 GV point the lowest values (slowest decays) of Figure 1 are used.

(A color version of this figure is available in the online journal.)

rigidity dependence of κ, which is very nearly proportional to rigidity P.

Taking into account that the values of λ_0 calculated from the model fits of Figure 9(a) are for $P_{\rm med} \approx 2$ GV, the rigidity dependence found in Figure 10 implies a diffusion mean free path for GLE 42 given by the range $\lambda = (0.17-0.2)P(\mathrm{GV})r(\mathrm{AU})^{0.9}$ AU. Since the initial phase of GLE 69 was not diffusive, one cannot calculate a similar range of values.

The difference in radial dependence of λ can be understood by noting that GLE 42 occurred in a relatively quiet period, while GLE 69 occurred during a large Forbush decrease with amplitude 15% on the Sanae neutron monitor, that had started three days prior to the event. For the quiet conditions of GLE 42 one can expect a mean free path that increases with radial distance. For GLE 69, however, enhanced turbulence generated at the sun three days prior to the GLE could have propagated to 1 AU and beyond at the time of the GLE, leading to a smaller λ there than at the Sun.

The magnitude of the diffusion mean free path derived for GLE 42 is in the range of the Palmer consensus mentioned above. The value also agrees reasonably well with that derived for the modulation of galactic cosmic rays via the simplest possible spherically symmetric Force-Field model. For solar minimum conditions, Caballero-Lopez & Moraal (2004) derived a modulation function $M = \int_{r_e}^{r_b} (V/\kappa)dr = 1.22/\beta P(\mathrm{GV})$ or Force-Field parameter $\varphi = M/3$. If κ and λ are independent of radial distance, this implies that $\lambda = 0.4\beta P(\mathrm{GV})$ AU. At solar maximum conditions, as pertained during the time of GLE 42, the value should be about half as much, i.e., $\lambda = 0.2\beta P(\mathrm{GV})$ AU. The nondependence on radial distance is justified by the fact that the Voyager spacecraft observed a radially independent radial gradient of 1%/AU at solar minimum to 2%/AU at solar maximum, measured from 1 to >100 AU (e.g., Moraal 2013). Such a constant gradient implies that κ and λ are independent of radial distance. This galactic cosmic-ray value of λ is representative of the perpendicular mean free path, $\lambda_\perp$, at $r \gg 1$ AU. The GLE-derived value should, however, be interpreted as representative of $\lambda_\parallel$ at $r < 1$ AU,

In the case of very large anisotropy such as in the beginning phase of GLE 69, the diffusive approximation is, of course, not valid at all. In this case, the so-called focused transport equation is solved, usually in one dimension (along the background magnetic field). This procedure has been described in detail by Ruffolo et al. (2006) and references therein. This equation specifies the intensity as function of pitch angle relative to the field direction, and it includes both adiabatic cooling and focusing in this diverging field. It then calculates the particle intensity and anisotropy relative to the field. In this way, several GLEs have been modeled as due to a single pulse released on or near the sun, with the anisotropy deviations and complicated time profiles being due to propagation effects in disturbed magnetic fields such as reflection off a scattering region beyond 1 AU (Lovell et al. 1998 and references therein), a magnetic bottleneck (Bieber et al. 2002) or a closed interplanetary magnetic loop (Ruffolo et al. 2006). As far as we know this focused-transport model has not been applied to GLEs 42 and 69.

The anisotropy of GLE 42 is discussed in the next section.

8. ANISOTROPY

The two main effects that determine the time profile of a GLE are its rigidity spectrum and its anisotropy. An understanding of the rigidity spectrum requires knowledge of the anisotropy. In its beginning stages, the event is usually highly anisotropic because the particles propagate as a beam along the magnetic field line from their solar source to Earth. This beam gets scattered in the field irregularities so that the anisotropy gradually decreases with time. The multiple stations in the neutron monitor network

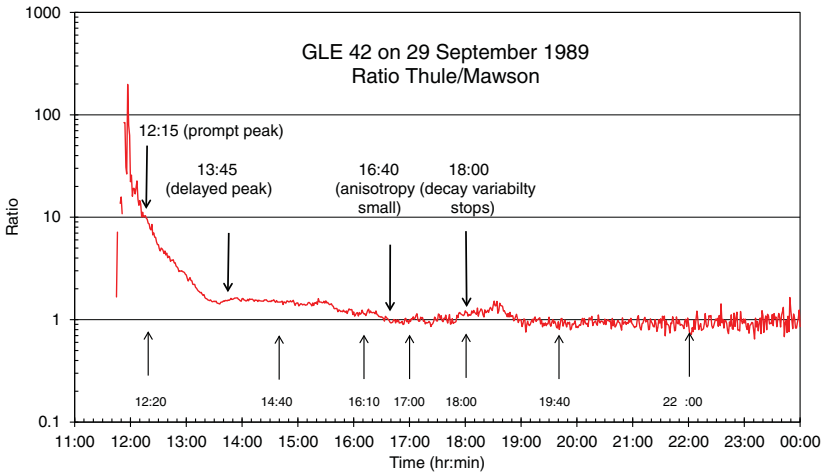

Figure 11. Anisotropy of the event expressed by the ratio of the increases at Thule and Mawson, respectively, the fastest and slowest risers. These two stations had 1 minute resolution. At 11:57 it reaches its maximum value of 220. At 12:15, when the peak intensities are observed for the prompt stations (red stations in Figure 2), this ratio has dropped to 10. At 13:45 when the delayed increases reach their maximum, the ratio has fallen to 1.5. The anisotropy almost disappears at 16:40, then slowly grows again, and from ≈18:40 onwards it finally remains insignificant. The upward arrows are the times for which the spectra in Figures 17 and 18 are calculated.

(A color version of this figure is available in the online journal.)

are well-suited to observe and interpret this anisotropy because each of these stations has a unique viewing direction into space. This is not the zenith direction above each station, because the particles are deflected by the geomagnetic field. Therefore, the asymptotic direction of viewing for a given station is defined as that direction outside the geomagnetic field from which a particle has to come in order to arrive from the vertical direction at the station. These asymptotic directions are calculated by numerical integration of the Lorentz force law $\boldsymbol{F} = q(v\mathrm{x}\boldsymbol{B})$, starting at the station point on Earth, using the opposite charge sign, and then tracing the trajectory of the particle until it is effectively outside the geomagnetic field (typically at 25 Earth radii). The technique was developed by McCracken (1962a, 1962b) and extensively used by Shea, Smart and many others (see, e.g., Smart et al. 2000; also Cooke et al. 1991). A neutron monitor that views asymptotically in the direction of the oncoming beam will see the earliest and steepest rise, while stations looking the other way will observe a delayed rise toward maximum intensity, because they can only see particles after they have been sufficiently scattered so that they start to arrive from the opposite direction.

Figure 11 displays the anisotropy of the event as the ratio of the increases on Thule, the fastest riser, to Mawson, the slowest riser. This ratio jumps up fast so that at 11:57 it reaches its maximum value of 220. This represents a highly focused beam of particles. At 12:15, when the peak intensities are observed for the prompt stations (red stations in Figure 2), this ratio has dropped to 10, which is still highly anisotropic. (We note that the time resolution is one minute—on a five minute running average basis, the maximum amplitude of 195% at 11:57 would be reduced to 60%.) These "large" anisotropies are moderate, however, when compared to GLE 69, where the anisotropy in the first few minutes was so large that it cannot be quantified. At 13:45, when the delayed peaks reach their maximum, the ratio has fallen to 1.5. The anisotropy almost disappears at 16:40 and then grows moderately again. At ≈18:00, it disappears permanently and, as can be seen from Figure 1, the variability of the decay also stops at this point.

The asymptotic directions of viewing for several stations with cutoff rigidity $P_c < 1$ GV are shown in Figure 12. The stations

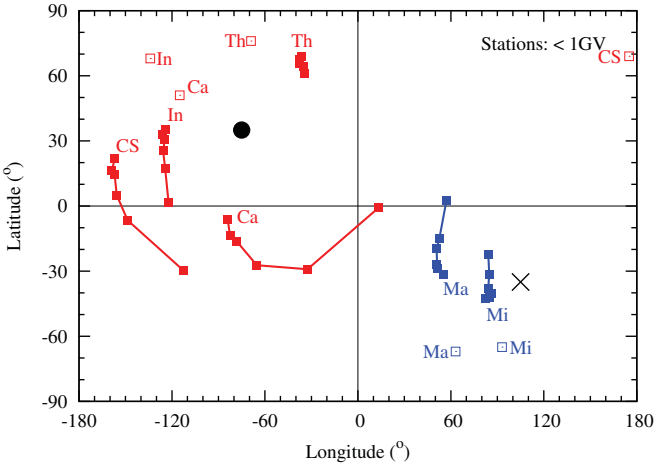

Figure 12. Asymptotic directions of viewing for four neutron monitors (Calgary, Cape Schmidt, Inuvik, and Thule) that saw the largest and most rapid increase. Also shown (in blue) are Mawson and Mirny which saw the slowest rise. The full symbols are arrival directions for $P = 6$, 5, 4, 3, 2, and 1 GV. The station name appears nearest to the 6 GV point. The estimated direction and anti-direction of arrival at ≈12:15 are marked with • and X, respectively. The open symbols are at the station location.

(A color version of this figure is available in the online journal.)

chosen are the ones most relevant to determine the direction of GLE 42. For each station there are six points. They are the asymptotic directions of arrival for particles with rigidities 1–6 GV, in intervals of 1 GV. The point nearest to the geographic position of the detector is the 6 GV point (because its trajectory has been bent least). Trajectories for rigidities below a certain value are not allowed because they either intersect with Earth, or the particles remain stuck in the magnetosphere. This defines the cutoff rigidity, with details and refinements of the concept, such as a penumbral range of rigidities above the final cutoff, described in, e.g., Smart et al. (2000). The bending is such that the asymptotic directions of arrival are typically deflected equatorward of the position of the neutron monitor. Bieber et al. (2004) used this concept of different viewing directions to develop a network of neutron monitors (in which some existing

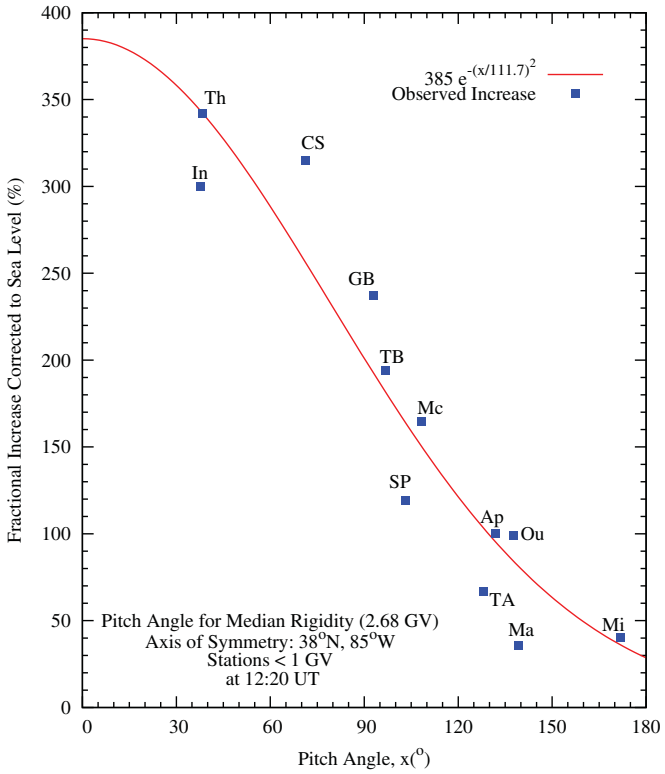

Figure 13. Increases at 12 stations as function of the angle from the weighted axis of symmetry of the event.

(A color version of this figure is available in the online journal.)

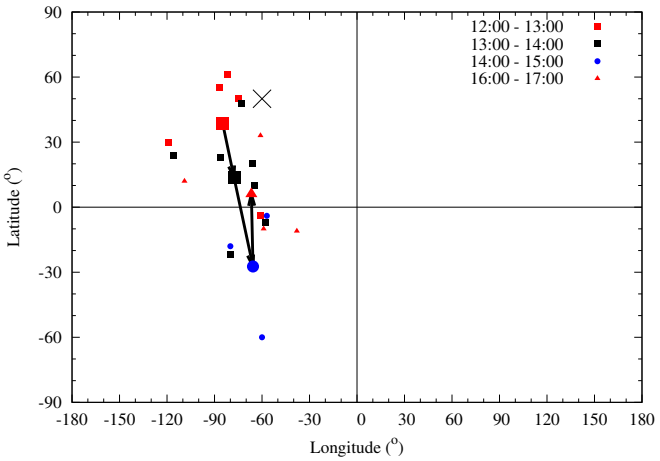

Figure 14. Axis of symmetry derived from asymptotic directions of viewing such as in Figure 12. The data are taken from Miroshnichenko et al. (2000). Small symbols are the arrival directions reported in previous works during that time interval, and the large ones are the average. The event came from between 70° and 90°W and remained there, but it shifted considerably in latitude. The *X* is the direction of the heliospheric magnetic field at Earth estimated by Smart & Shea (1991).

(A color version of this figure is available in the online journal.)

neutron monitors were relocated), for their "Spaceship Earth" network. The two stations with the least latitudinal bending toward the equator are Thule in the North and McMurdo in the South. Hence, these two stations are considered to be the "polar directions" in the Spaceship Earth concept.

The anisotropy in Figure 11 therefore indicates that the beam arrived near to the asymptotic direction of viewing of Thule, while the anti-direction was near to the asymptotic direction of Mawson.

In the calculation presented here, we used the International Geomagnetic Reference Field (IGRF) for 1995, e.g., Sabka et al. (1997). More refined calculations, such as those of Duldig et al. (1993), Lovell et al. (1998), Ruffolo et al. (2006), and references therein, use higher-order field models such as the Tsyganenko (1989) model. These models also allow for secular variations in the geomagnetic field due to disturbed conditions in the heliospheric magnetic field and the solar wind. Such refinements cause moderate variations in the asymptotic directions, as shown by, e.g., Duldig et al. (1993), and variations of up to ±20% in cutoff rigidities; they are not expected to cause substantial differences in our conclusions.

The anisotropy calculation is refined by considering the increases at other stations to find a weighted optimal axis of symmetry. This is shown for 12 stations in Figure 13 at the time of the prompt peak at 12:15. The fitted curve through the points is a Gaussian with an opening angle (the angle where the increase is 1/e of its maximum value) of $111\overset{\circ}{.}7$, and the direction of maximum intensity is 38°N, 85°W. This distribution is almost identical to that found by Duldig et al. (1993) and Lovell et al. (1998). These variations are not important for our interpretations.

Miroshnichenko et al. (2000) tabulated 21 such arrival directions, calculated at various times during the event by, e.g., Kolomeets et al. (1991), Morishita et al. (1991), Cramp et al. (1993), Duldig et al. (1993), de Koning & Bland (1995), and Dvornikov & Sdobnov (1995). These arrival directions are shown in Figure 14. The averages of these estimates are indicated by the larger symbols. It shows that the asymptotic direction of the event stayed within the range of 60°–90°W, but that it shifted from latitude 38°N to 30°S at about 15:00, and then shifted northward again. The nominal direction of the heliospheric magnetic field as estimated by Smart & Shea (1991) is shown with an X.

This anisotropy is much smaller than that calculated by McCracken et al. (2012) for GLEs 8, 31, and 69 that occurred on 1960 May 4, 1978 May 7, and 2005 January 20, respectively, and which were characterized by a two-peak profile. As mentioned before, the anisotropy in the beginning of GLE 69 is so large that it is difficult to express it quantitatively.

The anisotropy also provides a further understanding of the possible two-peak structure of the event, as inferred by Miroshnichenko et al. (2000). For this purpose Figure 15 shows an enlargement of the early phases of Figure 2, which highlights the time variability of the increases. Among the different traces, there are four that are shown in green, and that show two peaks, with the first one at ≈12:15. They are Goose Bay, Deep River, Tixie Bay, and Calgary. Inuvik, which shows a large increase in the interval ≈13:15–13:25, is also shown in green. The previous arguments about a double-peak event, plus other significant time variations are mainly based on the time profiles of these selected stations. Miroshnichenko et al. (2000) summarized these interpretations by proposing that the HMF during the event had the shape of a giant loop, with both ends rooted in the Sun. Hence, the particles could be injected into both ends of the loop. If the path lengths along the two sides of the loop are different, it will naturally lead to two increases. This concept is quantitatively and graphically described by Ruffolo et al. (2006).

However, it is clear from Figure 15 that these stations were by no means the only ones that saw a complicated or two-peak

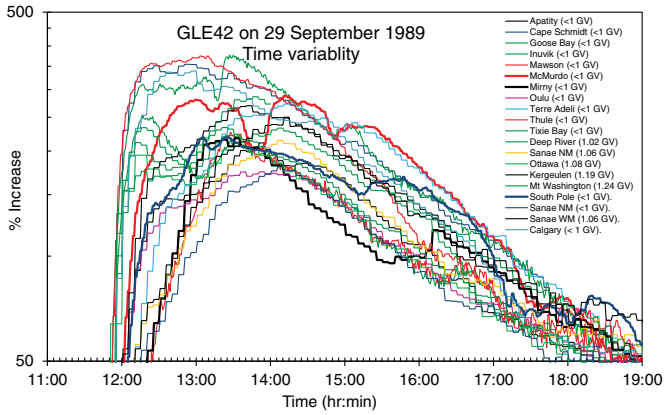

Figure 15. Time profiles of $P_c < 1.24$ GV stations during the first half of the event. The figure is an expansion of Figure 2. It highlights the large variability during the first half of the event.

(A color version of this figure is available in the online journal.)

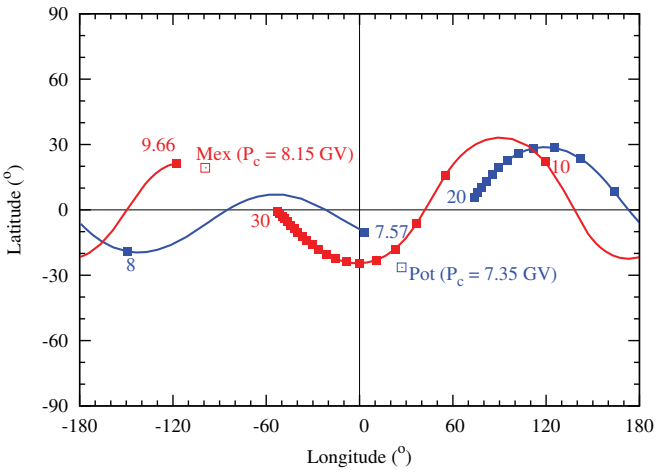

Figure 16. Asymptotic directions of viewing for Potchefstroom, $P_c = 7.35$ GV, and Mexico, $P_c = 8.15$ GV. Points are from 20 and 30 GV downward in interval of 1 GV. In contrast to Figure 13, these stations receive particles over a wide range of longitudes, and they are therefore much less sensitive to anisotropy. From the lowest rigidity point plotted to the cutoff rigidity for each station, the "tail" of the distribution goes around the Earth more than once.

(A color version of this figure is available in the online journal.)

time structure. Some examples are McMurdo (red) that showed a large dip at ≈13:50, and then two high excursions between ≈14:00 and 15:00. Mirny (thick black) had the lowest increase up to ≈15:30, but then showed a sudden sharp increase between 15:30 and 16:00, and another one just after 18:00. South Pole (thick blue) also saw an abrupt increase at ≈15:10. Closer inspection reveals many more, smaller variations of this kind, and they do not form a specific pattern in time. These fluctuations have periods as short as a few minutes. We note that in a typical 5 nT heliospheric magnetic field at Earth, the gyroradius of a (typical) 5 GV GLE proton is ∼0.01 AU, and its gyroperiod is ∼1 minute. According to Weygand et al. (2011), the correlation length of the field is of the same order of magnitude, hence one expects a fairly unstable beam of particles, with the instability increasing with the degree of anisotropy. Thus, the time profiles of the green stations may possibly indicate a double-peak event as suggested by Miroshnichenko et al. (2000), but we argue that it is more likely that the large variability is due to oscillations in the arrival direction of the beam, as it continuously shifted according to the changing direction of the HMF. The argument is supported by similar, but larger and more rapid fluctuations observed by Bieber et al. (2013) in GLE 69 on 2005 January 20.

We also examine the anisotropy observed by stations with cutoff rigidity $P_c > 1$ GV. Figure 16 shows asymptotic directions of viewing for Mexico City and Potchefstroom, with cutoff rigidities of 8.15 and 7.35 GV. They are typical examples of >1 GV stations. For Potchefstroom the plotted arrival directions are shown in 1 GV intervals from 20 to 8 GV, and for Mexico City from 30 GV to 10 GV. For rigidities <7.57 GV at Potchefstroom and <9.66 GV at Mexico City, down to the cutoff rigidity, the arrival directions tend to spread out even further and "snake" around the earth (not shown). In contrast to the <1 GV stations in Figure 12, these stations therefore receive particles over a wide range of longitudes. Since the spectra are steep, the biggest contribution occurs in the 1–2 GV interval above the cutoff rigidity. Therefore, stations with increasingly higher cutoff rigidities are progressively less sensitive to the anisotropy. This is qualitatively seen in Figure 3: with increasing P_c the increases not only become smaller and decay more rapidly, but there is also progressively less time variation in the decay phase, because the instruments receive particles over a wide range of longitudes. We note that the second group of stations in Figure 3, the late risers Durham, $P_c = 1.41$ GV, Moscow, $P_c = 2.46$ GV, Newark, $P_c = 1.97$ GV, Kiel $P_c = 2.29$ GV, and Novosibirsk, $P_c = 2.91$ GV, are the highest-rigidity stations that show a sensitivity to the anisotropy.

This analysis also provides an explanation for the slow increase and decay of the Moscow muon telescope in Figure 4. The three $P_c < 1$ GV muon telescopes have fairly narrow cones of acceptance so that the asymptotic directions of arrival generally lie within 60° from the inferred axis of symmetry in Figure 12. On the other hand, the Mt. Norikura and Nagogy arrival directions are widely spread in longitude, but the direction for 13–15 GV particles also lies within 60° from this axis. The arrival directions for Moscow are similarly spread in longitude, but here the most sensitive interval (∼15 GV) lies from about 90° to 120° East, which is much nearer to the anti-direction in Figure 12. However, the direction for ≈2.5 to 3 GV particles once again passes within 60° of the axis of symmetry, and it is therefore these low-rigidity particles that are detected. Since the muon telescope is relatively insensitive to these low rigidities, the peak intensity is practically at the same level as that of the high-cutoff stations Mt. Norikura and Nagoya. Finally, using the rigidity dependence of Figure 10, it also explains why the decay is much slower than for the other muon telescopes.

9. RIGIDITY SPECTRUM

Figures 17 and 18 show the spectra of this event at seven different times. These times are indicated with upward arrows in Figure 11. The individual data points are read off from the increases in Figures 1 and 2. The curves are calculated with the procedure outlined in Caballero-Lopez & Moraal (2012). This entails that the counting rate N of a neutron monitor at cutoff rigidity P_c and atmospheric depth x is calculated from $N(P_c, x) = \int_{P_c}^{\infty} S(P, x) j(P) dp$. The yield function $S(P, x)$ is given in that paper. For the galactic cosmic-ray background, N_g, the spectrum $j(P)$ above the atmosphere is that observed by Earth-orbiting satellites, while for the solar energetic particles the counting rate, N_s, is calculated for power-law spectra of the form $j \propto P^{-\gamma}$. The fractional increase $\delta N/N$ is then given by the ratio N_s/N_g. The spectral indices γ that produce these increases are shown in the individual panels. The fractional increases $\delta N/N$ are corrected to what they would have been at sea level,

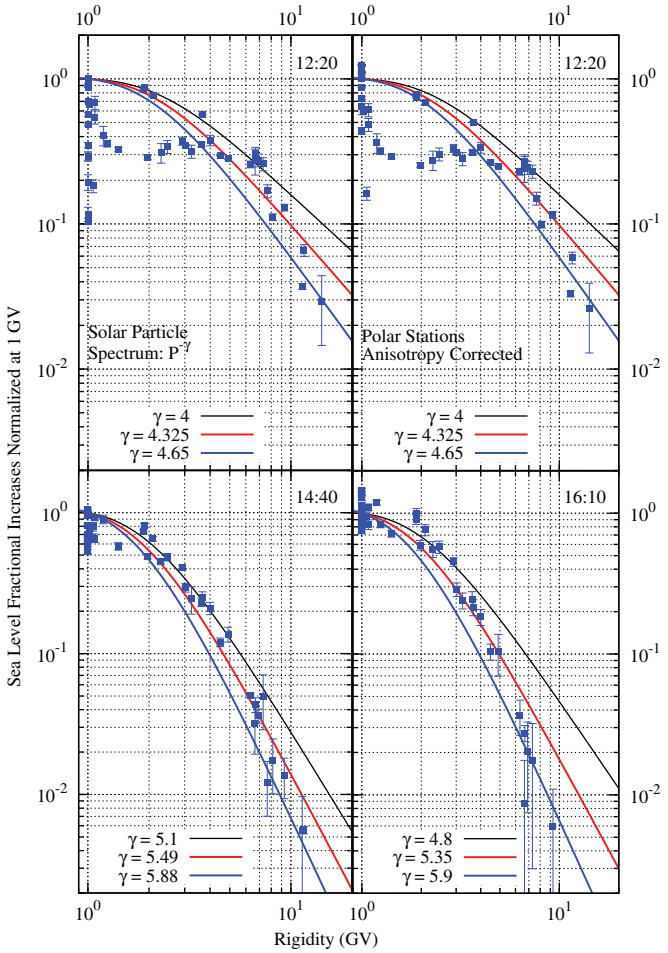

Figure 17. Estimated power-law spectra of the form $P^{-\gamma}$ for the event at 12:20, 14:40, and 16:10. The three lines on each panel are for three different power-law indices. The top two panels show the increases without (left) and with (right) correction for anisotropy, but only for the <1 GV stations. The observed fractional increases are corrected to the values at sea level, and are normalized to the increase at Thule (effectively at 1 GV). The error bars are calculated from the statistical variation on the increase in a given time interval (5 minutes in most cases).

(A color version of this figure is available in the online journal.)

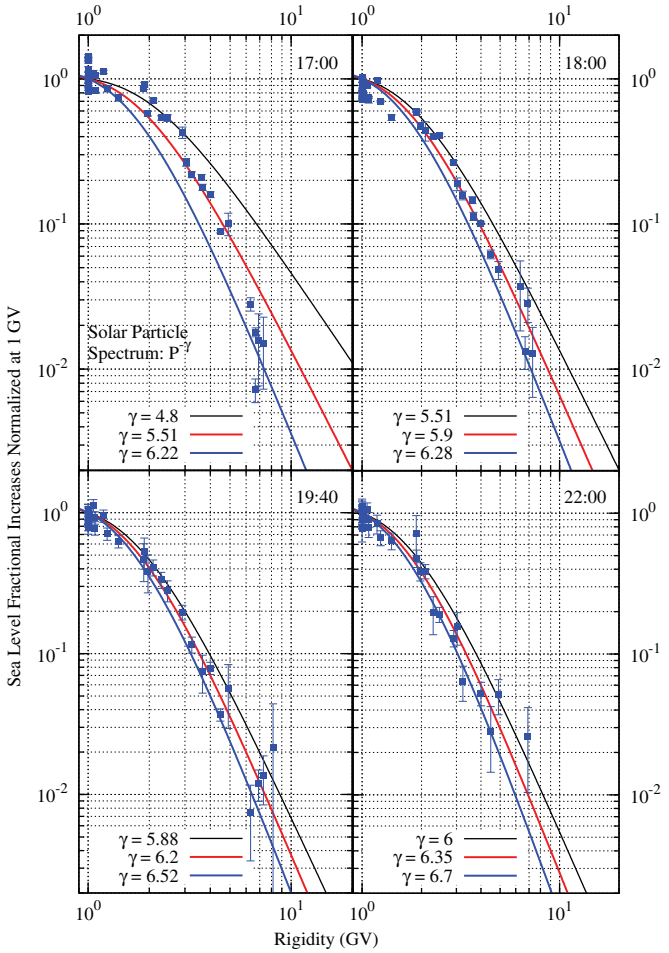

Figure 18. Same as Figure 17, but for the later times 17:00, 18:00, 19:40, and 22:00.

(A color version of this figure is available in the online journal.)

and normalized to the fastest and largest increase in the event, which is for Thule. The procedure is to use the NM yield function of Caballero-Lopez & Moraal (2012) and a power law for the solar particle spectrum to calculate the fractional increase for a given value of the spectral index. Then this calculated increase is used to correct to sea level the observed increase at altitude x. Finally, the corrected sea level increase is normalized to its value for Thule. Thus the points in these two figures represent the plotted $\delta N/N =$ (observed $\delta N/N/\delta N/N$ at Thule) $\times$ ($\delta N/N$ at P_c, sea level)/($\delta N/N$ at P_c, x), while the curves are the sea level calculated increase.

The overall trend is that in the course of the event the spectral index evolves from ≈4 to >6.

In the top left panel of Figure 17, there is a wide range (about 10) in the magnitude of increases at $P_c = 1$ GV. It also shows a concave "loop" effect for stations with $1 < P_c < 3$ GV. These two effects are due to the strong anisotropy in the beginning stages of the event. The "loop" is deceptive. It is not a systematic effect, because there are three points in this interval where the increases are "high." They are for the top three curves in Figure 3, namely, Hobart, $P_c = 1.88$ GV; Mt. Wellington, $P_c = 1.89$ GV; and Magadan, $P_c = 2.09$ GV.

For $P_c > 2$ GV this anisotropy effect becomes progressively smaller due to the properties of the asymptotic cones of acceptance for high-cutoff stations discussed with Figure 16. Moving to later times in the event, represented in the subsequent panels in Figures 17 and 18, this anisotropy effect also diminishes, as expected.

The top right-hand panel of Figure 17 is a repetition of the left-hand panel, but with the increases at 1 GV corrected for anisotropy effects as outlined in Section 8 above. (The points for $P_c > 1$ GV have not been corrected.) Now the range of increases at 1 GV has been reduced from a factor of 10 (ranging from 0.1 to 1) to a factor of 2.8 (from 0.44 to 1.23). This implies that the anisotropy correction is only partially successful. The reason is that the individual station points in Figure 13 deviate from the fitted curve by up to a factor of 2.8.

In Sections 2 and 7, we used the relatively gradual increase to maximum intensity as an indicator that the particles were accelerated in a CME shock. Hence, we now interpret the spectral form in terms of the theory of shock acceleration.

First-order *Fermi*, or shock acceleration produces power-law spectra with spectral index γ determined by the compression ratio s of the shock. The relationship is $\gamma = (s + 2)/(s - 1)$ or $s = (\gamma + 2)/(\gamma - 1)$. This implies that in the beginning

stages of the event, when $\gamma \approx 4$, the compression ratio $s \approx 2$. When γ has increased to ≈7 late in the event, the shock strength has decreased to $s \approx 1.5$. The strongest possible shock has $s = 4$, which should produce a spectrum with $\gamma = 2$. The observations thus imply that if the particles were accelerated in the envelope-shock of a CME, this shock was relatively weak. The compression ratio s is the ratio of the upstream to downstream velocity relative to the shock front. If the shock moves with speed $V_s \approx 1800$ km s^{-1} and the ambient solar wind speed is 400 km s^{-1}, then the upstream speed relative to the shock is 1400 km s^{-1}. Thus, to produce a P^{-4} spectrum (for $s = 2$) early in the event, this implies that the speed of the ejecta behind the shock was ≈700 km s^{-1}.

The spectra are not clear power laws, however. In three cases, at 12:20, 16:10, and 17:00, they fall off faster than a power law, so that they can be better represented by an exponential spectrum of the form $\exp(-P/P_o)$. Most of the previous studies, cited in Miroshnichenko et al. (2000), have proposed such exponential spectra. This exponential fall-off is, however, less distinct at 14:40, 18:00, 19:40, and 22:00, i.e., the spectra remain much nearer to power-law form up to the highest rigidities. Thus the time development of the spectrum is unclear within the statistical uncertainties of the measurements.

Lovell et al. (1998) showed spectral information of the event at energies below the sensitivity range of neutron monitors. From observations in the range 2–200 MeV nucleon^{-1} by IMP 8, and *GOES* 6, 7, and 8, they found that both the proton and alpha particle kinetic energy spectra are of the form T^{-2} during the first hour of the event. Such a kinetic energy spectrum in this nonrelativistic energy range is equivalent to a rigidity spectrum of the form of P^{-3} (not P^{-4}; see, e.g., Moraal 2013). This spectrum is significantly harder than the spectra in the beginning phases of the event in Figure 17, which suggests that there are further spectral effects outside the neutron monitor rigidity range.

In first-order *Fermi* acceleration, the power-law spectral form is maintained for those rigidities where the radius of curvature of the shock is larger than the diffusive length scale, κ/V_s. If we use the range of values $\kappa = 4 \times 10^{15} \beta P$ cm^2 s^{-1} to $\kappa = 4 \times 10^{18} \beta P$ cm^2 s^{-1} derived in Section 4, and $V_s \approx 1800$ km s^{-1}, the diffusive length scale κ/V_s ranges from $0.0003 \beta P$ to $0.3 \beta P$ solar radii, with P expressed in GV. This is much smaller than the radius of curvature of the shock which is always significantly larger than one solar radius. Hence, one does not expect an exponential cutoff in the rigidity range of Figures 17 and 18. Even from this comprehensive study we can, therefore, not claim to understand the spectrum of the event in detail.

Figure 19 summarizes the spectral information deduced from this, and several previous studies. The seven blue symbols toward the top are the values calculated from Figures 17 and 18. Points with other colors are from references as indicted on the figure. Our derived spectral index tends toward the high range of these previous calculations, and they are in best agreement with those of de Koning (1994).

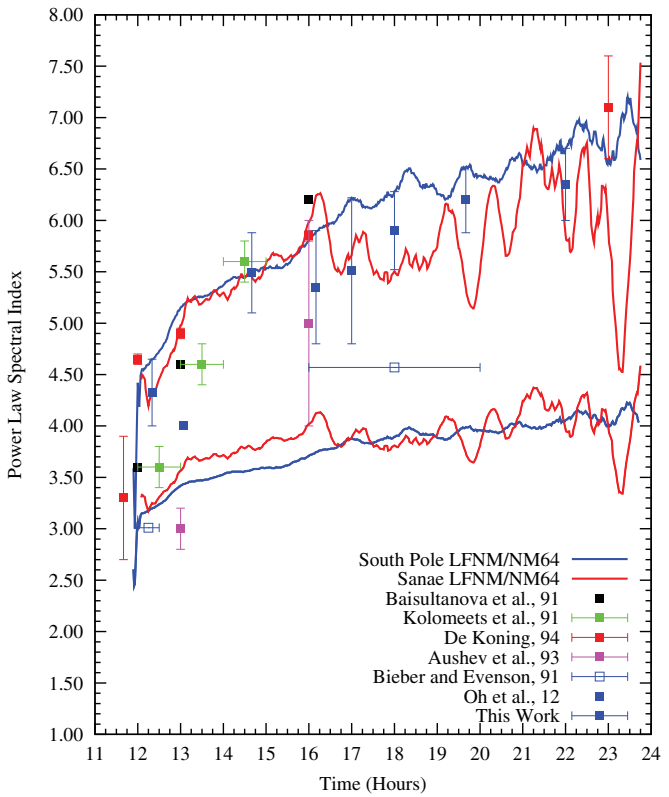

Figure 19. Power-law spectral indices for the event. Our blue points are compared with several previous calculations. The continuous lines are calculated from ratios of increases of lead-free neutron monitors (LFNM) to standard neutron monitors. The top two curves use the LFNM yield function of Aleksanyan et al. (1979), and the bottom two that of Stoker (1995). The data points are from Aushev et al. (1993), Baisultanova et al. (1991), Bieber & Evanson (1991), De Koning (1994), Kolomeets et al. (1991), Oh et al. (2012).

(A color version of this figure is available in the online journal.)

10. SPECTRA CALCULATED FROM LEAD-FREE NEUTRON MONITORS

There is a useful supplementary way to determine the spectral form of GLEs. It is based on the counting ratio of a lead-free neutron monitor (LFNM) to that of a standard neutron monitor at the same site. On average, the former responds to somewhat lower energy particles, so that the ratio of the two is an indication of the spectral shape of the observed increases. Technically, the yield function for a LFNM is somewhat skewed to lower rigidities relative to that for a standard neutron monitor.

There are two such continuously running LFNMs. The one at Sanae has been in operation since 1971. Oh et al. (2012) recently demonstrated the ratio method for 12 large GLEs, going back to GLE 42 by using the South Pole pair of detectors.

The technique is powerful because the pair of detectors respond to exactly the same environmental conditions, and it therefore requires no corrections for variations or uncertainties in these conditions. Second, the method is almost anisotropy-free, because they view in the same asymptotic direction. (There will, of course, always be a small anisotropy residual left, because particles with different rigidities come from different directions, and the median rigidity of response is not exactly the same. This effect, however, is estimated to be much smaller than other uncertainties.)

The four continuous curves in Figure 19 represent the spectral index as calculated from the counting ratio of the LFNMs to standard neutron monitors, N_{lf}/N_{NM}, at South Pole (blue) and Sanae (red). The top two are based on the atmospheric yield function, $S(P,x)$, for the LFNMs derived by Aleksanyan et al. (1979), and the bottom two with that of Stoker (1995). We did not explicitly use the LFNM yield functions calculated in these papers: both papers published the ratio of the LFNM counting rate to that of an NM64 neutron monitor. We thus multiplied our yield function for the NM64 neutron monitor

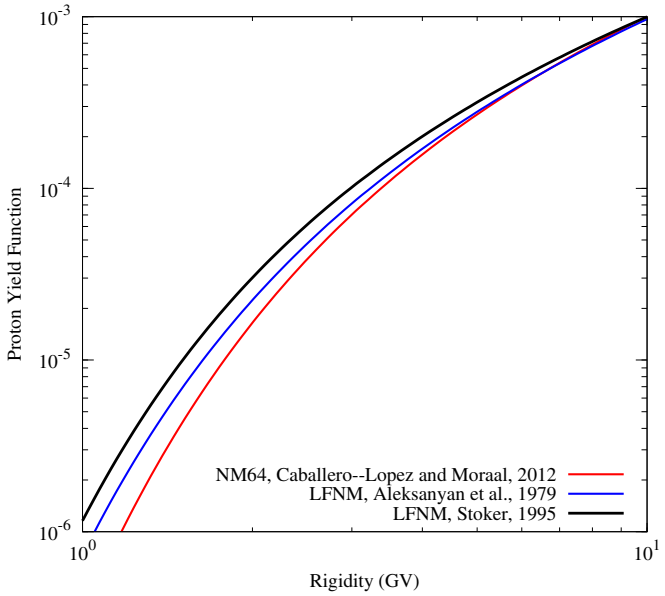

Figure 20. Yield functions used in this work for the calculation of the spectral index shown by the full lines in Figure 19.

(A color version of this figure is available in the online journal.)

derived in Caballero-Lopez & Moraal (2012) with the ratio of the differential response function for the LFNM relative to the neutron monitor to find a yield function for the LFNMs. We follow this ratio procedure because we have confidence in our newly derived neutron monitor yield function.

Next, we calculated the fractional increases for the LFNMs in the same way as was done for neutron monitors in Figures 17 and 18. This ratio is a function of γ. This calculated ratio was compared to the observed ratio to determine the values of γ plotted in Figure 19.

We note that the values for South Pole and Sanae are in fair agreement. There seem to be fluctuations on the Sanae curves. These are not systematic but due to the fact that the curves are running average fits through individual data points, and the statistical fluctuations are larger at Sanae than at South Pole.

The values derived with the LFNM yield function of Aleksanyan et al. (1979) are in excellent agreement with those derived from the neutron monitor increases in Figures 17 and 18 and the values of de Koning (1994). However, the values of γ derived from the Stoker yield function are much smaller than those of Aleksanyan et al., and also much smaller than those derived from neutron monitors. This is due to the fact that the two yield functions differ significantly. This is shown in Figure 20. Although the differences seem to be small, the difference between the Aleksanyan and Stoker yields is of the same order of magnitude as the difference between the LFNM and the neutron monitor, and they are large enough to lead to the discrepancy in Figure 19.

Because the method is inherently powerful and accurate, this discrepancy calls for an accurate re-measurement of the lead-free neutron monitor yield function.

The same principle can be applied by using pairs of nearby standard neutron monitors at different altitudes. In this case, the higher instrument sees the softer spectrum, similar to the LFNM. Examples of pairs we have tried are Hobart and Mount Wellington, Alma Ata A and C, and Mount Washington and Newark. The results were inconclusive, however, and this is probably due to different environmental conditions for which one cannot correct in sufficient detail.

11. SUMMARY AND CONCLUSIONS

Ground-Level Enhancement 42 of 1989 September 29 is the most outstanding example of a "classical" GLE in the database of 71 such events observed since 1942. It was observed by more neutron monitors and muon telescopes than any other GLE because (1) it had a very hard spectrum so that it was detected by a multitude of high-cutoff detectors, and (2) the number of ground-based detectors peaked during that era.

According to the recent grading of Bieber et al. (2013), the event was only seventh biggest of 71 such GLEs. This classification is based on the peak intensity, which favors events with an impulsive, prompt peak before the main phase of the event sets in (see, e.g., McCracken et al. 2012). Here we note that the main phase of GLE 42 was actually the second biggest, after GLE 05 of 1956 February 23. That GLE was, however, observed by only 12 instruments (those in the database), while GLE 42 was observed by 58.

Because the spectrum was so hard and long-lasting, the event offers almost unique opportunities to study it as a prototype for GLEs. By the time of this investigation, it had been studied in at least 76 previous other papers, but from our strategy to include all the available information, we make several new contributions. They are as follows.

1. The event is the archetypical example of the "classical" GLE that has a rise time of 30–60 minutes. Based on the discussions in papers such as Vashenyuk et al. (2006, 2011) and McCracken et al. (2008, 2012), we infer that it was caused by the acceleration of particles in the CME shock associated with the event. Previous papers, such as Miroshnichenko et al. (2000) and references therein, have identified a more complicated, multiple-peak structure that is due to more than one acceleration, injection and/or propagation path to Earth. Due to our simultaneous use of all the available data, we suggest that such fluctuations are more likely due to fluctuations in the heliospheric magnetic field during the event, which cause directional instabilities in the anisotropic beam.
2. The very well resolved time structure of the event, especially its tail, enables one to fit a simple diffusive profile to the event, and derive a diffusion mean free path in the range $\lambda = (0.17\text{–}0.20)P(\mathrm{GV})r(\mathrm{AU})^{0.9}$ AU. The range in magnitude reflects the anisotropy of the event. This is in general agreement with the value derived for the modulation of galactic cosmic rays. De Koning & Mathews (1996) found a similar value at 1 GV, but their derived rigidity dependence was linear, instead of the current power-law form. The diffusive nature and the rigidity dependence of the diffusion coefficient support the diffusive shock acceleration/CME origin of the event.
3. The nature of the event as described in the previous point is strengthened by showing that GLE 69 of 20 January 2005 cannot be similarly interpreted. This event has a very large, prompt initial peak, and an anisotropy in its initial phases that was orders of magnitude larger.
4. The acceleration during the first two or three minutes of GLE 42 was not due to diffusive shock acceleration in the CME. The reason is that the small time dispersion of the initial increases over the large rigidity range from $\approx$1 to more than 30 GV implies that the diffusion coefficient

would have to be at least two orders of magnitude smaller than can be inferred from other means. Hence, we consider the particles produced during these first minutes as due to a process lower in the corona, likely to be associated with the flare.

5. In combination, GLEs 42 and 69 can be understood as that in both of them there was an initial, prompt acceleration, lasting only a few minutes. Thereafter there was a more gradual acceleration lasting several tens of minutes to more than an hour. It is natural that the initial acceleration will be a pre-acceleration for the second boost. In GLE 42 the effect of the prompt, initial acceleration as observed at Earth, was weak because the disturbance on the sun and its assumed associated flare were hidden behind the western limb. However, the ensuing CME had a very large angular extent, so that the particles accelerated in this second boost were readily detectable at Earth. In the case of GLE 69, the flare site at $\sim 60^{\circ}$W was almost perfectly connected to Earth via the Parker spiral magnetic field, so that the promptly accelerated particles were very well visible at Earth, while those that were accelerated by the secondary mechanism remained engulfed below these particles until about an hour into the event.
6. Our anisotropy studies of the event do not reveal new information over and above what has been published before. The review of Miroshnichenko et al. (2000) remains an excellent source of this anisotropy information. One contribution is that the anisotropy disappears at rigidities >2 GV because of the nature of asymptotic cones of acceptance in Earth's magnetic field. This has been known all along, but because the spectrum was so exceptionally hard, the effect is seen much clearer than in other GLEs.
7. Our spectral determinations are fairly standard, but, once again, we have extended previous work by including all available information. We find that our spectral estimation is in good agreement with that of de Koning (1994), but it is softer than determined in several other studies. We remark that even for this event, with the hardest, best observed spectrum of all GLEs, it is still difficult to calculate a precise spectrum. For instance, we could not firmly differentiate between power-law and exponential form.
8. We confirm several previous arguments of McCracken et al. (2008), Bieber et al. (2005), and Oh et al. (2012) that the use of lead-free neutron monitors is a very sensitive and highly reliable tool to determine the spectral shape of GLEs. However, the results derived from this method differ significantly according to the yield function for the lead-free monitor in the literature. The main reason is that these yield functions are insufficiently known, particularly in the rigidity range <3 GV. To improve this, renewed latitude surveys with pairs of neutron monitors and lead-free monitors should be done.

This work was supported by South African NRF grant SNA2011110300007 and Mexican PAPIIT-UNAM grant IN110413. Both authors acknowledge the hospitality of the University of Maryland where part of the work was performed in 2012. The neutron monitor observations used are from the worldwide network, collected in the database described in McCracken et al. (2012). This database originated from the work of Shea et al. (1985, 1987), it was managed by Shea, Smart, and Gentile (e.g., Gentile 1993) until 1999, and updated and migrated by M. L. Duldig (Duldig & Watts 2001), E. A. Eroshenko, and H. Moraal. It is currently available at http://usuarios.geofisica.unam.mx/GLE_Data_Base. We thank the referee for many constructive suggestions.

REFERENCES

Aleksanyan, T. M., Blokh, Ya. L., Dorman, L. I., & Starkov, F. A. 1979, in Proc. 16th Int. Cosmic Ray Conf., ed. S. Miyake (Vol. 4; Tokyo: Univ. Tokyo), 321
Alessio, M., Allegri, L., Fargion, D., et al. 1991, NCimC, 14, 53
Aushev, V. M., Dorman, L. I., Kryakunova, O. N., et al. 1993, in Proc. 23rd Int. Cosmic Ray Conf., ed. D. A. Leahy (Vol. 3; Calgary: World Scientific), 75
Baisultanova, L. M., Belov, A. V., Dorman, L. I., et al. 1991, in Proc. 22nd Int. Cosmic Ray Conf., ed. D. O'Sullivan (Vol. 3; Dublin: Inst. Adv. Studies), 105
Bhatnagar, A., Jain, R. M., Burkepile, J. T., et al. 1996, Ap&SS, 243, 209
Bieber, J. W., Clem, J. M., Evenson, P. A., et al. 2005, in Proc. 29th Int. Cosmic Ray Conf., ed. B. Sripathi et al. (Vol. 1; Mumbai: Tata Inst. Fund. Res.), 237
Bieber, J. W., Clem, J. M., Evenson, P. A., et al. 2013, ApJ, 771, 92
Bieber, J.W., Dröge, W., Evenson, P. A., et al. 2002, ApJ, 567, 622
Bieber, J. W., & Evenson, P. A. 1991, in Proc. 22nd Int. Cosmic Ray Conf., ed. D. O'Sullivan (Vol. 3; Dublin: Inst. Adv. Studies), 129
Bieber, J. W., Evenson, P. A., Ruffolo, D., et al. 2004, ApJL, 601, L103
Burkepile, J. T., & St. Cyr, O. C. 1993, NCAR Technical Note, NCAR/TN-369 + STR, Boulder, CO
Caballero-Lopez, R. A., & Moraal, H. 2004, JGR, 109, A01101
Caballero-Lopez, R. A., & Moraal, H. 2012, JGR, 117, A12103
Caballero-Lopez, R. A., Moraal, H., & McDonald, F. B. 2004, JGR, 109, A05105
Chupp, E. L., Debrunner, H., Flückiger, E., et al. 1987, ApJ, 318, 913
Cliver, E. W., Kahler, S. W., & Vestrand, W. T. 1993, in Proc. 23rd Int. Cosmic Ray Conf., ed. D. A. Leahy (Vol. 3; Calgary: World Scientific), 91
Cooke, D. J., Humble, J. E., Shea, M. A., et al. 1991, NCimC, 14, 213
Cramp, J. L., Duldig, M. L., & Humble, J. E. 1993, in Proc. 23rd Int. Cosmic Ray Conf., ed. D. A. Leahy (Vol. 3C; algary: World Scientific), 47
De Koning, C. A. 1994, Master's thesis, Univ. Calgary, Calgary, Alberta
De Koning, C. A., & Bland, C. J. 1995, in Proc. 24th Int. Cosmic Ray Conf., ed. N Iucci & E. Lamanna (Vol. 4; Rome: IUPAP), 212
De Koning, C. A., & Mathews, T. 1996, CaJPh, 74, 290
Drury, L. 1983, SSRv, 36, 57
Duldig, M. L., & Watts, E. J. 2001, in Proc. 27th Int. Cosmic Ray Conf., ed. H. Kampert et al. (Vol. 8; Berlin: Copernicus), 3409
Duldig, M. L., Cramp, J. L., Humble, J. E., et al. 1993, in Proc. A.S.A., 10, 211
Duggal, S. P. 1979, RvGSP, 17, 1021
Dvornikov, V. M., & Sdobnov, V. E. 1995, in Proc. 24th Int. Cosmic Ray Conf., ed. N Iucci & E. Lamanna (Vol. 4; Rome: IUPAP), 236
Gentile, L. C. 1993, JGR, 98, 21107
Giacalone, J., & Jokipii, J. R. 1999, ApJ, 520, 204
Gosling, J. T. 1993, JGR, 98, A18937
Kolomeets, E. V., Sevost'yanov, V. N., Chebakova, E. A., & Seleznev, K. B. 1991, Bull. Acad. Sci. USSR, Phys. Series 55, 24
Lovell, J. L., Duldig, M. L., & Humble, J. E. 1998, JGR, 103, A23733
MacQueen, R. M., Eddy, J. A., Gosling, J. T., et al. 1974, ApJL, 187, L85
McCracken, K. G. 1962a, JGR, 67, 423
McCracken, K. G. 1962b, JGR, 67, 435
McCracken, K. G. 1962c, JGR, 67, 447
McCracken, K. G., Moraal, H., & Shea, M. A. 2012, ApJ, 761, 101
McCracken, K.G., Moraal, H., & Stoker, P.H. 2008, JGR, 113, A12101
Miroshnichenko, L.I., de Koning, C.A., & Perez- Enriquez, R. 2000, SSRv, 91, 615
Moraal, H. 2013, SSRv, 176, 299
Moraal, H., Belov, A., & Clem, J. M. 2000, SSRv, 93, 285
Moraal, H., & McCracken, K. G. 2012, SSRv, 171, 85
Morishita, I., Nagashima, K., & Sakakibara, S. 1991, in Proc. 22nd Int. Cosmic Ray Conf. (Vol. 3; Dublin: Inst. Adv. Studies), 121
Ng, C. K., & Reames, D. V. 2008, ApJL, 686, L123
Oh, S. Y., Bieber, J. W., Clem, J. M., et al. 2012, SpWea, 10, S05004
Palmer, I. D. 1982, RvGSP, 20, 335
Parker, E. N. 1965, P&SS, 13, 9
Ruffolo, D., Tooprakai, P., Rujiwarodom, M., et al. 2006, ApJ, 639, 1186
Sabka, T. J., Langel, R. A., Baldwin, R. T., & Conrad, J. A. 1997, JGG, 49, 157
Shea, M. A., & Smart, D. F. 1996, in AIP Conf. Proc. 374, ed. R. Ramaty et al. (Melville, NY: AIP), 131
Shea, M. A., & Smart, D. F. 1997, in Proc. 25th Int. Cosmic Ray Conf., ed. M. S. Potgieter (Vol. 1; South Africa: Potchefstroom Univ.), 129
Shea, M. A., & Smart, D. F. 2000, SSRv, 93, 229

Shea, M. A., Smart, D. F., Humble, J. E., et al. 1987, in Proc. 20th Int. Cosmic Ray Conf., ed. V. A. Kozyarivsky et al. (Vol. 3; Moscow: Nauka), 171
Shea, M. A., Smart, D. F., Wada, M., & Inoue, A. 1985, in Proc. 19th Int. Cosmic Ray Conf., ed. F. C. Jones et al. (Vol. 5; Washington, DC: NASA), 510
Smart, D. F., & Shea, M. A. 1991, in Proc. 22nd Int. Cosmic Ray Conf., ed. D. O'Sullivan (Vol. 3; Dublin: Inst. Adv. Studies), 101
Smart, D. F., Shea, M. A., & Flückiger, E. O. 2000, SSRv, 93, 305
Smart, D. F., Shea, M. A., Wilson, M. D., & Gentile, L. C. 1991, in Proc. 22nd Int. Cosmic Ray Conf., ed. D. O'Sullivan (Vol. 3; Dublin: Inst. Adv. Studies), 97
Stoker, P. H. 1995, SSRv, 73, 327
Takahashi, K., Wada, M., Sakamoto, E., et al. 1990, Proc. Japan Acad. Series B, 66, 10
Tousey, R. 1973, in Space Res. Conf., ed. M. J. Rycroft & S. K. Runcorn (Vol. 2; Berlin: Akademic-Verlag), 713
Tsyganenko, N. A. 1989, P&SS, 37, 5
Vashenyuk, E. V., Balabin, Y., & Gvozdevsky, B. 2011, ASTRA, 7, 459
Vashenyuk, E. V., Balabin, Y., Perez-Peraza, J., et al. 2006, AdSpR, 38, 411
Vashenyuk, E. V., Miroshnichenko, L. I., Sorokin, M. O., et al. 1994, AdSpR, 14, 711
Weygand, J. M., Matthaeus, W. H., Dasso, S., & Kivelson, M. G. 2011, JGR, 116, A08102